



# Ilmenite and magnetite microfabrics in shocked gneisses from the Vredefort impact structure, South Africa

Fabian Dellefant<sup>1</sup> · Claudia A. Treppmann<sup>1</sup> · Stuart A. Gilder<sup>1</sup> · Iuliia V. Sleptsova<sup>1</sup> · Melanie Kaliwoda<sup>1,2</sup> · Benjamin P. Weiss<sup>3</sup>

Received: 18 February 2022 / Accepted: 27 July 2022 / Published online: 5 September 2022  
© The Author(s) 2022

## Abstract

We investigated microfabrics of shocked Archean gneisses from two, 10 m-deep drill cores located near the center of the Vredefort impact structure in an area that is characterized by a prominent, long-wavelength negative magnetic anomaly ( $< -3000$  nT) together with short-wavelength, high-amplitude anomalies attributed to lightning strikes. Planar fractures and feather features in quartz, which can be partially recrystallized, indicate shock conditions less than 20 GPa. Micrometer-sized magnetite and ilmenite along shock-related shear fractures in quartz and feldspar emanate from adjacent deformed coarse ( $> 100$   $\mu\text{m}$ ) ilmenite and magnetite host grains. These fine-scaled veins suggest mobilization of magnetite and ilmenite during shear deformation of host Fe-phases and adjacent silicates, probably associated with frictional heating. Coarse ilmenite has fine-lamellar mechanical twins parallel to  $\{10\bar{1}1\}$  and single (0001) twins, indicative of dislocation-glide-controlled deformation under non-isostatic stresses related to shock. A few  $\mu\text{m}$ -wide magnetite lamellae parallel to  $\{10\bar{1}1\}$  and spheroidal magnetite (diameter  $\approx 10$   $\mu\text{m}$ ) within coarse ilmenite document exsolution after shock. Dauphiné twins associated with planar features in quartz imply cooling from 650 to 725 °C after shock, which accords with estimates of pre-impact basement temperatures from petrographic studies. The Curie temperature of magnetite is 580 °C; therefore, the central negative magnetic anomaly was produced as a thermoremanent magnetization acquired during cooling of the initially hot crust. The long-wavelength anomaly was likely amplified by the newly created magnetite that also acquired a thermal remanence. Although the magnetic properties of surface samples are often influenced by lightning strikes, we found no microstructural evidence for lightning-related processes.

**Keywords** Shock effects · Ilmenite twins · Magnetite exsolution · Magnetite and ilmenite veins · Frictional heating · Planar fractures

## Introduction

Large meteorite impacts impart rapid stress changes onto the target rocks during shock loading and subsequent unloading; elevated temperature conditions as well as changes in redox

conditions prevail over longer time scales (Melosh 1989; Migault 1998; Nesterenko 2001; Sharp and DeCarli 2006). Upon these changes, the microstructures of the target rocks are permanently modified. Minerals undergo phase transformation (e.g., melting, amorphization, exsolution) and deformation (e.g., fracturing, twinning) on different time scales throughout the cratering process. We refer to “shock” for all processes that affect the target rocks during impact cratering and to “shock effects” for the resulting microstructures. The microstructural changes influence the magnetic properties of ferrimagnetic minerals within impact structures, leading to distinct km-scale magnetic field anomalies (Fig. 1) (Pilkington and Grieve 1992; Scott et al. 1997; Plado et al. 1999; Pilkington and Hildebrand 2000; Ugalde et al. 2005; Pohl et al. 2010). However, the effect of shock pressure, shock-generated heat, and post-shock modifications on magnetic

---

Communicated by Timothy L. Grove.

---

✉ Fabian Dellefant  
fabian.dellefant@lmu.de

<sup>1</sup> Department of Earth and Environmental Sciences, Ludwig-Maximilians-University, Munich, Germany

<sup>2</sup> Mineralogical State Collection, SNSB, Munich, Germany

<sup>3</sup> Department of Earth, Atmospheric and Planetary Sciences, Massachusetts Institute of Technology, Cambridge, MA, USA

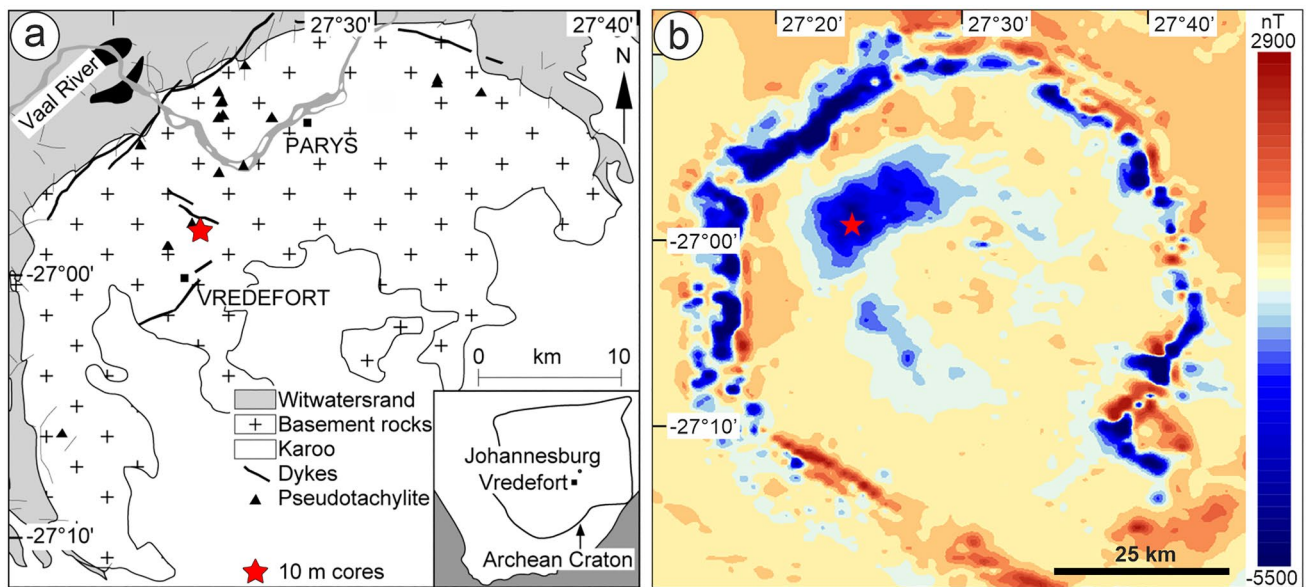


**Fig. 1** **a** Simplified geological map of the Vredefort impact structure (modified after Nel 1927 and Carporzen et al. 2012). **b** Sample location (red star) in the aeromagnetic anomaly map based on data of

Antoine et al. (1990) and Corner et al. (1990); modified after (Gilder et al. 2018). Sample location is shown by red star

minerals are poorly understood (Reznik et al. 2016, 2017; Gilder et al. 2018).

Lightning strikes can also effect magnetic minerals by rapidly changing temperature and redox conditions (Rakov and Uman 2003; Salminen et al. 2013). The magnetic fields produced by lightning are typically characterized by high Koenigsberger ratios, defined as the ratio of the natural remanent magnetization (NRM) to the magnetization induced by Earth's magnetic field (Koenigsberger 1938). Furthermore, lightning-induced magnetic fields can be characterized by ratios of the NRM divided by a saturating isothermal remanent magnetization that approach 1 (Kletetschka et al. 2004). As a result, long-lived crustal magnetic fields can be generated by lightning that extend a few m to several tens of m, displaying gradients of up to tens of nT/m (Sakai et al. 1998; Verrier and Rochette 2002; Appel et al. 2006; Shimizu et al. 2007).

The Vredefort impact structure is characterized by large, km-scale ( $> 1000$  nT) magnetic anomalies (Hargraves 1970; Hart et al. 1995; Muundjua et al. 2007; Carporzen et al. 2012). Moreover, the surface is subjected to frequent lightning strikes (Gijben 2012), which includes the area northwest of the center, which possesses a km-scale negative magnetic anomaly (red star in Fig. 1) superimposed on the short-wavelength anomalies due to lightning. Single-domain (SD) magnetite observed within planar shock effects in quartz from this location has been related to both the impact shock event (Grieve et al. 1990; Hart et al. 1991; Cloete et al. 1999) and lightning strikes (Carporzen et al. 2012). Carporzen et al. (2012) showed that samples from

two 10 m-deep drill cores up to 100 cm below the surface exhibit dual Verwey transition temperatures (120–130 and 90–110 K) and high remanent coercivities ( $\approx 40$  mT). The population with higher Verwey transition temperatures and lower coercivities was ascribed to original, Archean multi-domain (MD) magnetite, while the fraction with lower Verwey transition temperatures and higher coercivities was ascribed to lightning strikes. At depths below the influence of lightning overprinting, the magnetization was interpreted as a thermoremanent magnetization acquired in the geomagnetic field following impact at 2.02 Ga (Carporzen et al. 2012).

The samples drilled within the high-amplitude anomaly of the shocked Archean basement rocks within the Vredefort Dome described by Carporzen et al. (2012) offer an ideal occasion to evaluate microstructural differences within rocks from the same locality (i.e., at similar shock conditions) to distinguish the local influence of lightning or meteorite impact on magnetite and ilmenite microfabrics and on the magnetic properties, which is the aim of this study.

## Geological overview

The Vredefort Dome lies in the Witwatersrand Basin, central Kaapvaal Craton, South Africa ( $27^{\circ} 00' S$ ,  $27^{\circ} 30' E$ , Fig. 1), centered approximately 120 km southwest of Johannesburg. It is a deeply eroded, 80–90 km diameter structure formed by a meteorite impact at ca. 2.02 Ga (Spray 1995; Kamo et al. 1996; Gibson et al. 1997). A 40–50 km central

region of Archean amphibolite- to granulite-facies migmatitic gneiss is surrounded by a 15–20 km wide collar of late Archean to early Proterozoic rocks (Armstrong et al. 1991). The oldest age estimated from the gneiss is 3.6 Ga based on a comparison to the Barberton basement rocks (Compston and Kröner 1988; Hart et al. 1990; de Wit et al. 1992; Zeh et al. 2011). The upper amphibolite- to granulite-facies metamorphism in the core region occurred at 3.09–3.07 Ga, with the metamorphic grade increasing towards the center of the structure, consistent with increasing levels of central uplift during impact cratering (Hart et al. 1999, 2004; Perchuk et al. 2002; Lana et al. 2003, 2004; Gibson 2019). Various migmatitic to more restitic gneisses (Hart et al. 1990; Stepto 1990) occur, which represent variable amounts of melt segregation, migration, and fractionation (Lana et al. 2003, 2004). Metamorphism of the surrounding lower Witwatersrand Supergroup sediments occurred at mid-amphibolite to greenschist facies conditions and is dated to about 2.9–2.7 Ga (Armstrong et al. 1991).

The original diameter of the impact structure is estimated to be 250–300 km based on geophysical modeling (Henkel and Reimold 1998), remote sensing (Phillips et al. 1999), as well as empirical relations of central uplift diameter to rim diameter, the spatial distribution of pseudotachylyte, and concentric large-scale structural patterns (Therriault et al. 1997). The amount of erosion is estimated to be 8–11 km as constrained by geobarometric analyses (Gibson et al. 1998) and geophysical considerations (Henkel and Reimold 1998); McCarthy et al. (1990) estimated 5–10 km of erosion occurred since impact based on regional stratigraphic studies. Fluid inclusions along shock-induced planar deformation features (PDFs) indicate trapping at depths of 7–15 km (Fricke et al. 1990). Together with an assumed structural uplift of about 3–12 km and an erosion of 8–11 km, the rocks exposed today in the central region were estimated to have been at depths of about 11–23 km before the impact (Gibson et al. 1998, 2019).

The prolonged thermal history of the exposed exhumed deep part of the Vredefort structure has considerably modified the shock effects which obscure estimates of the pressure conditions acting during impact (e.g., Schreyer and Medenbach 1981; Fricke et al. 1990; Grieve et al. 1990; Gibson and Reimold 2005). In the center of the dome, quartz is largely recrystallized, where at increasing distance from the center, the amount of recrystallized grains decreases and new grains are aligned along strings within coarse host grains, which are interpreted to represent annealed planar features (Lilly 1981; Schreyer and Medenbach 1981; Fricke et al. 1990; Grieve et al. 1990; Reimold 1990; Hart et al. 1991; Leroux et al. 1994). Microstructural evidence based on shock effects in feldspar suggests that shock conditions were locally very heterogeneous, with maximum shock pressures in the central parts of the dome exceeding 30–35 GPa,

and locally more than 45 GPa, decreasing to about 10 GPa at a 20 km distance from the center (Gibson and Reimold 2005).

One of the largest known magnetic anomalies found in a terrestrial impact structure is a km-scale ring of negative anomalies ( $< -5500$  nT) surrounding the crystalline bedrock at Vredefort (Fig. 1). The ring has been attributed to ferruginous shales of the Witwatersrand Group (Corner et al. 1990). Strongly negative ( $< -3000$  nT) anomalies exist in the Archean basement rocks northwest of the impact structure's center, which were probably generated due to thermal overprinting when the field was in a reversed polarity state (Hargraves 1970; Antoine et al. 1990; Muundjua et al. 2007; Carporzen et al. 2012). The lack of negative anomalies closer to the impact structure's center can be explained by lithologies impoverished in magnetite and not from shock demagnetization (Hart et al. 1995; Carporzen et al. 2005). The rocks studied in this present contribution stem from the "central negative anomaly" about 10 km from the center of the structure (red star in Fig. 1).

## Sampling and methods

### Sampling

We investigated material from two  $\approx 10$  m deep bore holes (VRED2 and VRED3; Lat  $-26.970942^\circ$  Long  $27.388698^\circ$ ) drilled in 2008 in an area of high-amplitude magnetic anomalies within Archean basement rocks (Fig. 1), where a pronounced foliation dips nearly vertical (Lana et al. 2003; Carporzen et al. 2012). The VRED2 and VRED3 drill cores have diameters of 2.5 cm and lengths of 10.12 and 10.56 m, respectively. They were acquired using a Winkie drill at two sites located  $\approx 5$  m apart. VRED2 lies within a strongly negative geomagnetic anomaly (positive inclination, downward), whereas VRED3 lies in a locally strong positive geomagnetic anomaly (negative inclination, upward) (Carporzen et al. 2012). Three-component magnetic field measurements taken in a  $10\text{ m} \times 10\text{ m}$  grid at 0.55, 1.2, and 2.55 m height, together with paleomagnetic data from samples drilled at the same location on the surface, demonstrate that the magnetic anomalies were produced by a lightning strike whose line-currents travelled along the surface for  $> 20$  m (Carporzen et al. 2012). From each core, 10 samples were selected at the following depths below the surface:

**VRED2:** V2 1.f (6 cm), V2 2.5 (13 cm), V2 4.2 (33 cm), V2 10.e (83 cm), V2 46.1 (456 cm), V2 54.1 (574 cm), V2 66.4 (770 cm), V2 69.1 (809 cm), V2 71.f (861 cm), and V2 78.2 (1003 cm).

**VRED3:** V3 2.1 (5 cm), V3 3.6 (15 cm), V3 3.16 (26 cm), V3 6.1 (87 cm), V3 34.12 (384 cm), V3 46.1 (549 cm), V3



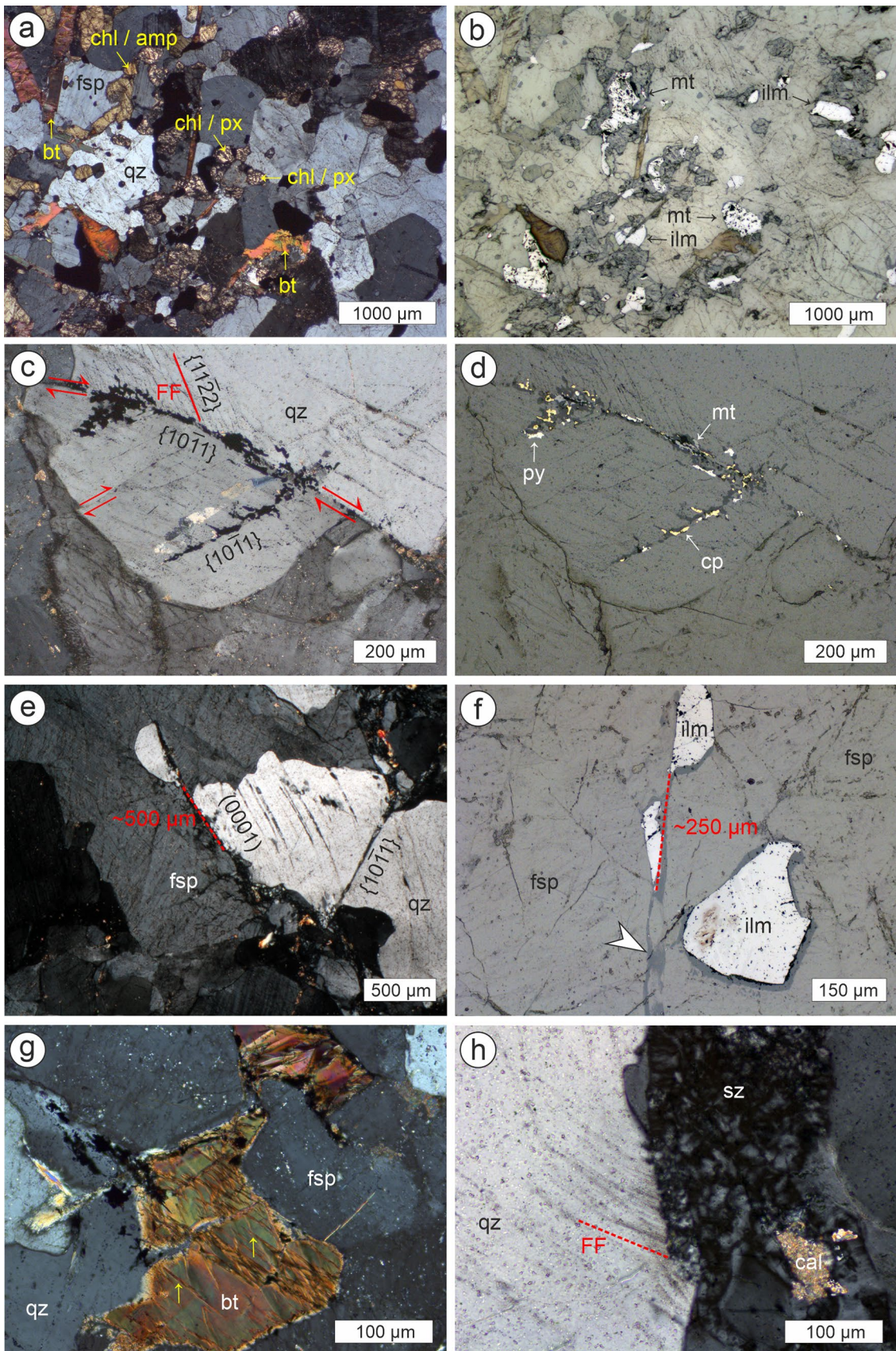




**Fig. 2** Polarized light photomicrographs of the sampled Archean gneisses. **a** Main rock-forming minerals quartz (qz), feldspar (fsp), biotite (bt), chlorite (chl), amphibole (amp), and pyroxene (px); transmitted light, crossed polarizers; sample V2 54.1 (574 cm depth). **b** Magnetite (mt) and ilmenite (ilm) in reflected light; sample V2 54.1 (574 cm depth). **c, d** Feather features (FFs) with shear offset (red double arrow) in quartz (qz). Along the shear fracture magnetite (mt), pyrite (py), and chalcopyrite (cp) occurs; **c** in transmitted light, crossed polarizers and **d** in reflected light; sample V2 4.2 (33 cm depth). **e** Transgranular shear fracture (red) in feldspar (fsp) and quartz (qz). Crossed polarizers; sample V3 60.5 (659 cm depth). **f** Sheared (red) ilmenite (ilm) along fracture (white arrow) within feldspar grains. Reflected light; sample V2 4.2 (33 cm depth). **g** Kink bands (yellow arrows) in biotite (bt) between quartz (qz) and feldspar (fsp). Crossed polarizers; sample V2 1.f (6 cm depth). **h** Shear zone (sz) with calcite (cal) in contact with a quartz grain (qz). Note the feather features (FF) emanating from the phase interface. Crossed polarizers; sample V2 78.2 (1003 cm depth)

60.5 (659 cm), V3 66.13 (769 cm), V3 67.3 (805 cm), and V3 73.4 (994 cm).

### Optical microscopy and universal stage measurements

Polished, uncovered thin sections (25  $\mu\text{m}$ ) were prepared from all samples and investigated by polarization microscopy (Leica DM2700 P) using both transmitted and reflected light. Photomicrographs were taken with a Leica MC170 HD camera and processed with the Leica Application Suite X 3.08.19082 software. A Leitz Universal-stage (U-stage) mounted on a Leitz optical microscope was used to determine the 3D orientation of the planar fractures (PFs) relative to the *c*-axis of the quartz. Uncertainty in the U-stage measurements is estimated at  $\pm 5^\circ$ ; undulatory extinction in quartz crystals may increase the uncertainty. The measurements are displayed in stereographic projections of the lower hemisphere. The crystallographic orientations of the PFs were derived by measuring the angle between the pole to the fracture and the *c*-axis (Stöffler and Langenhorst 1994; Trepmann and Spray 2005; Ferrière et al. 2009). The results from the U-stage were compared with crystallographic orientations in quartz measured by electron backscattered diffraction (EBSD).

### Scanning electron microscopy

Eight carbon-coated thin sections from V2 2.5 (13 cm), V2 4.2 (33 cm), V2 71.f (861 cm), V2 54.1 (574 cm), V3 2.1 (5 cm), V3 3.16 (26 cm), V3 34.12 (384 cm), and V3 60.5 (659 cm) were studied with a Hitachi SU5000 scanning electron microscope (SEM) equipped with a field emission gun, NordlysNano high-sensitivity EBSD detector (Oxford Instruments), energy-dispersive X-ray spectroscopy (EDS) detector (Oxford Instruments), and backscattered electron (BSE) detector. Full crystallographic orientation data

were obtained from automatically indexed EBSD patterns acquired with AZtec analysis software 4.2 (Oxford Instruments). For EBSD, thin sections were chemo-mechanically polished with a colloidal alumina suspension (Syton) to reduce the surface damage produced from preparation. SEM observations used accelerating voltages of 20 kV and working distances of 10–25 mm. Depending on the EBSD-pattern quality and resolution, step sizes for automatic mapping have been chosen between 0.5 and 2  $\mu\text{m}$ . We used a sample holder tilted at  $70^\circ$ . EBSD data were processed by the Channel software 5.12.74.0 (Oxford Instruments). All stereonets are equal-angle projections of the lower hemisphere.

### Raman spectroscopy

In situ Raman spectroscopy was carried out to identify the iron-bearing phases and feldspar in fine-grained aggregates with an HORIBA JOBIN YVON XploRa ONE micro Raman system at the Munich Mineralogical State Collection Munich (SNSB). The Raman spectrometer was equipped with edge filters and a Peltier-cooled CCD detector. A 1800 g/mm grate was used together with a green  $2\omega$ -Nd:YAG laser (532 nm) on iron-bearing phases in an attenuated mode (10% laser power) corresponding to max. 0.9 mW on the sample surface to avoid oxidation (Bauer et al. 2011; Kaliwoda et al. 2021), which could, for example, transform magnetite-to-hematite, thereby leading to a false interpretation. Hole and slit diameters were 300 and 100  $\mu\text{m}$ . An integration time of  $2 \times 16$  s was applied. For feldspar, the green laser was used in attenuation mode with 100% laser power corresponding to maximum 9.1 mW at the surface. Hole and slit were set to 300 and 200  $\mu\text{m}$  with counting times of  $3 \times 60$  s. A  $100\times$  long working distance objective resulted in a 0.9  $\mu\text{m}$  laser spot size on the sample surface. Wavelength calibration was performed with a pure Si wafer chip on the predominant  $520 \pm 1$   $\text{cm}^{-1}$  peak. The wave number reproducibility was checked several times a day and deviations were found to be less than 0.2  $\text{cm}^{-1}$ ; the precision in Raman peak position is estimated at  $\pm 1.5$   $\text{cm}^{-1}$ .

### Results

We first give a general description of the shocked Archean gneisses (Fig. 2) with shocked quartz crystals (Fig. 3) and associated occurrences of fine-grained quartz and feldspar aggregates (Figs. 2h, 4). We then describe ilmenite and magnetite deformation fabrics (Figs. 5, 6, 7, 8, 9), which is followed by a description of ilmenite and magnetite alteration microfabrics (Fig. 10). All observed microfabrics occur in

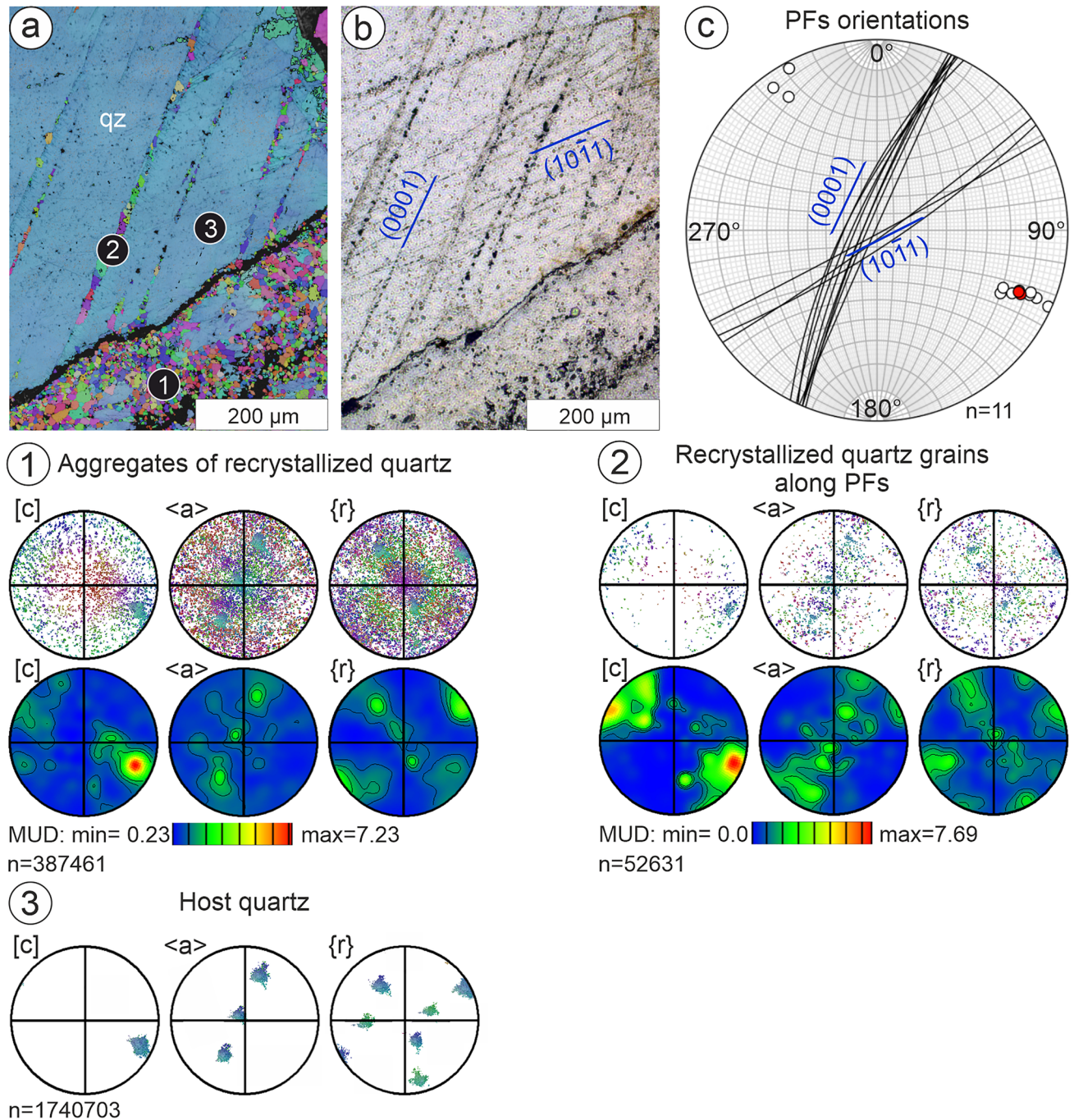


**Fig. 3** EBSD and U-stage data of shocked quartz, sample V2 2.5 (13 cm depth). **a** EBSD orientation map (inverse pole figure of  $z$ -direction), displaying aggregates of new grains (1) and new grains along PFs (2) within a host quartz (3). **b** Polarized light photomicrograph with the indicated orientation of the two sets of PFs parallel to (0001) and (1011). **c** Stereographic projections (lower hemisphere) of the PFs orientations (white) displayed in **b**, measured by U-stage.

The  $c$ -axis measurements are colored red. **1, 2** Pole figures and density plots of the  $c$ - and  $a$ -axes and poles to  $r$ -planes of the aggregates of new quartz and new quartz grains along PFs, respectively, stereographic projections (lower hemisphere), corresponding to the orientation map in **a**. **3** Pole figures of  $c$ - and  $a$ -axes and poles to  $r$ -planes of the host quartz in stereographic projections (lower hemisphere), corresponding to the orientation map in **a**



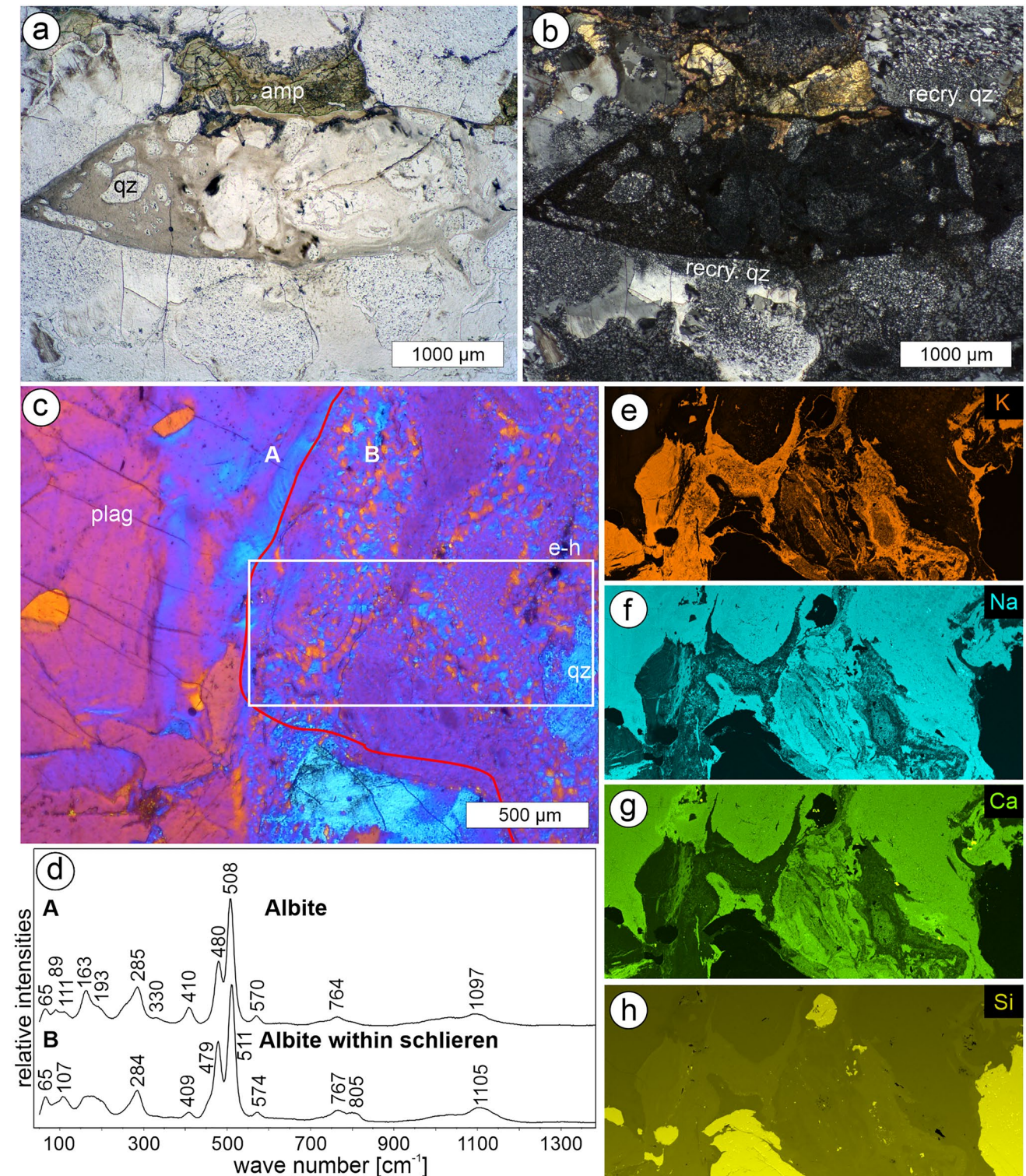


**Fig. 4** Polarized light photomicrographs, EDS data, and Raman spectra of fine-grained quartz and feldspar aggregates, sample V2 71.f (861 cm depth). **a, b** Schlieren microstructure in contact with an altered amphibole (amp) and recrystallized quartz (recry. qz). Image **b** taken with crossed polarizers. **c** Boundary (red) between shear zone and quartz (qz) and plagioclase grains (plag). A and B indicate the

Raman spots for the spectra displayed in **d**, whereas the white rectangle indicates the area scanned by EDS analysis shown in **e–h**. Crossed polarizers and lambda plate. **d** Raman spectra of an albite-rich plagioclase grain (A) and the albite-rich component of the vein matrix (B). **e–h** Distribution maps for K (**e**), Na (**f**), Ca (**g**), and Si (**h**)



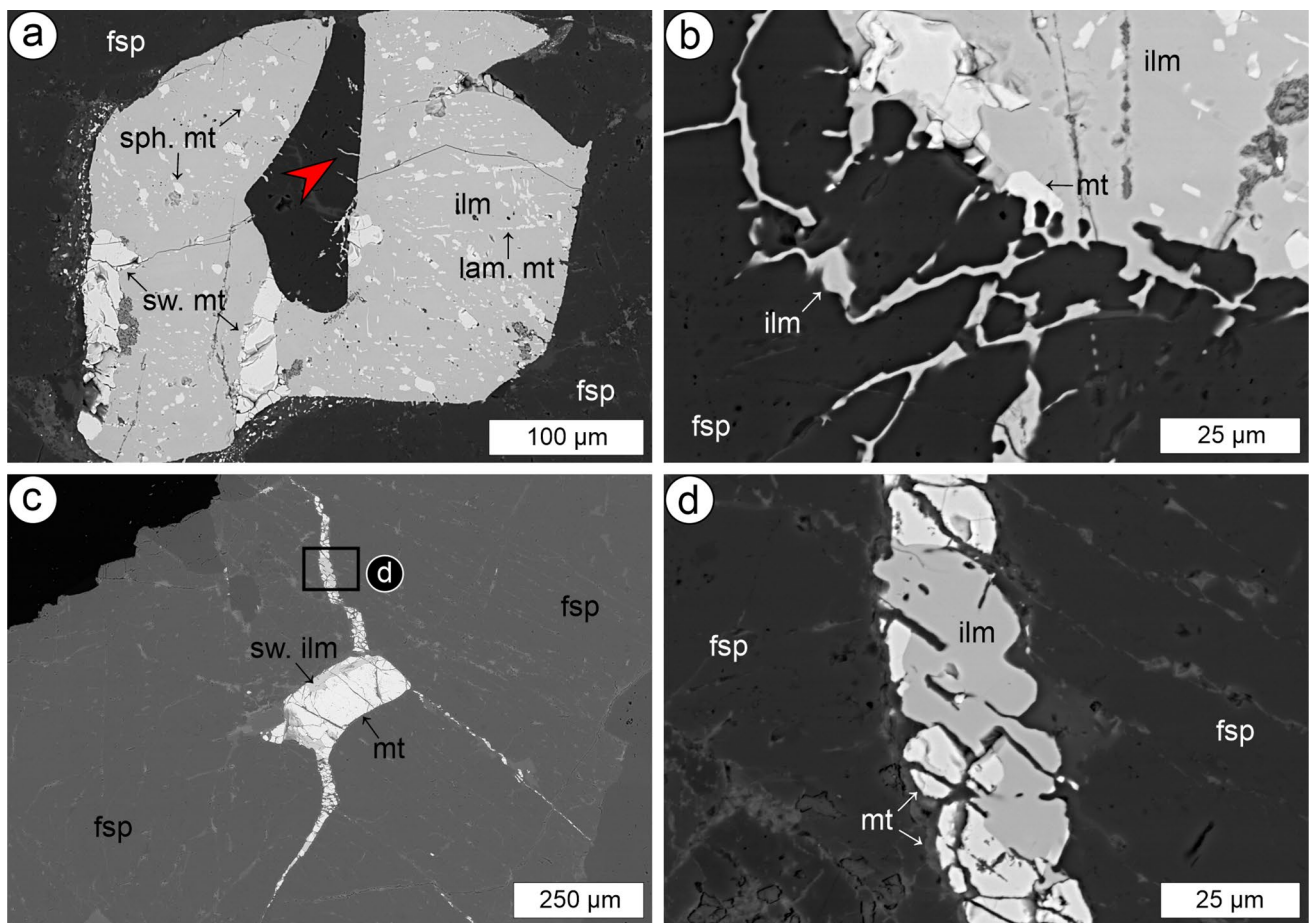


**Fig. 5** BSE images of ilmenite and magnetite microstructures. **a** Ilmenite (ilm)—magnetite (sw. mt) sandwich microstructure. Note lamellar (lam. mt) and spheroid (sph. mt) magnetite exsolutions. The red arrow indicates ilmenite along fractures in feldspar (fsp). **b** Ilmenite host grain (ilm) displaying intrusions composed of ilmenite and rarely magnetite (mt), which are located within fractured feldspar (fsp). Image **a** and **b** taken from sample V2 4.2 (33 cm depth).

**c** Coarse magnetite (mt) associated with ilmenite (sw. ilm) sandwich microstructure within feldspar (fsp). Magnetite and ilmenite occur along fractures in feldspar (sample V3 60.5, 659 cm depth). The area marked by the black rectangle is enlarged in **d**. **d** Ilmenite (ilm) and magnetite (mt) along a fracture in feldspar (fsp). Note the straight phase boundaries of magnetite and the rather curved ilmenite phase boundaries

both drill cores with a frequency that does not systematically vary with depth (Fig. 11).

### Sample description

Based on polarized light and electron microscopy, the investigated rocks are medium- to coarse-grained gneisses composed of 60–75% feldspar and 20–40% quartz (Fig. 2). Phyllosilicates occur up to 5% and consist of chlorite and biotite, which are commonly altered to chlorite and/or anatase. Pyroxene and amphibole are often chloritized (Fig. 2a). Opaque phases comprise 1–5% of the rock (Fig. 2b–d): iron/titanium oxides consist of  $\approx 70\%$  ilmenite and  $\approx 30\%$  magnetite, with minor pyrite and chalcopyrite (Fig. 2c, d). No hematite was identified in any sample. Anatase, calcite, zircon, and apatite often occur in direct contact with magnetite and/or ilmenite.

All minerals are fractured, especially quartz (Fig. 2c–e), feldspar, and ilmenite (Fig. 2f); shear fractures show offsets of several tens of  $\mu\text{m}$  (Fig. 2e, f). Biotite commonly displays kink bands (Fig. 2a, g). Quartz shows sets of crystallographically controlled, parallel fractures with a spacing of up to a few tens of  $\mu\text{m}$  (Figs. 2c–e, h, 3). These so-called PFs are well-known but non-diagnostic shock effects (Stöffler and Langenhorst 1994; French and Koeberl 2010; Stöffler et al. 2018). On one side of such fractures, second-order, fine-lamellar, sub-parallel fractures can emanate at high angles (Fig. 2c, d, h). These so-called feather features (FFs) are also common shock effects in quartz (Poelchau and Kenkmann 2011; Ebert et al. 2020). The central fractures of the FFs typically show a marked shear offset of tens of  $\mu\text{m}$  (Fig. 2c). When coarse magnetite and ilmenite are in contact with PFs and FFs of quartz or with fractures of feldspar, fine-grained



magnetite and ilmenite (and more rarely pyrite and chalcopyrite) occur within the shock features (Fig. 2c, d).

We measured the 3D orientation of PFs and FFs using a U-stage microscope in 18 grains from 10 samples [V2 1.f (6 cm), V2 2.5 (13 cm), V2 4.2 (33 cm), V2 46.1 (456 cm), V2 66.4 (770 cm), V3 2.1 (5 cm), V3 3.16 (26 cm), V3 34.12 (384 cm), V3 60.5 (659 cm), and V3 73.4 (994 cm)]. Figure 3 compares the U-stage and EBSD measurements to determine crystallographic orientations. We identified 26 sets, of which 15 were characterized as (0001) with 45 individual U-stage measurements, 9 as  $\{10\bar{1}1\}$  with 18 individual measurements, and one of each  $\{22\bar{4}1\}$  and  $\{11\bar{2}2\}$  with 2 individual measurements related to FFs. The PFs can be bent due to internal misorientation of the host quartz crystal (Fig. 2c, e).

About 30% of the quartz crystals are locally replaced by new grains (<2%) aligned along crystallographic planes parallel to (0001) and  $\{10\bar{1}1\}$  (Fig. 3), which are known quartz cleavage planes (Tröger 1982). About 20% of the PFs are decorated by secondary quartz grains. Partly recrystallized quartz in rocks from similar distances from the impact structure's center has been previously observed and interpreted to represent modified planar shock effects (e.g., Schreyer 1983; Fricke et al. 1990; Grieve et al. 1990; Reimold 1990; Leroux et al. 1994; Gibson and Reimold 2005). EBSD data show a large scatter in the crystallographic orientation of the new grains with a weak maximum close to the crystallographic orientation of the host quartz crystal, especially for the grains along PFs (Fig. 3a).

Fine-grained pure feldspar aggregates occur together with quartz replaced by new grains by about 50% (Figs. 2h, 4). These recrystallized quartz grains and fine-grained feldspar aggregates form few  $\mu\text{m}$  to 500  $\mu\text{m}$ -wide transgranular zones. In polarized light and SEM, the fine-grained feldspar aggregates show a schlieren microstructure composed of K-feldspar ( $\text{Or}_{79}\text{Ab}_{21}$ ) and plagioclase ( $\text{Ab}_{74}\text{An}_{26}$ ), as indicated by EDS (Fig. 4a–c, e–h) and Raman spectroscopy (Fig. 4c, d). Characteristic Raman peaks identified albite Si/Al–O bonds at  $284\text{ cm}^{-1}$ ,  $479\text{ cm}^{-1}$ ,  $511\text{ cm}^{-1}$ , and  $574\text{ cm}^{-1}$ , as well as peaks associated with Na–O and Ca–O vibrations (Mernagh 1991). The main peaks of Ab-rich plagioclase in direct contact with the schlieren microstructure display similar spectra with the main peaks at  $285\text{ cm}^{-1}$ ,  $480\text{ cm}^{-1}$ ,  $508\text{ cm}^{-1}$ , and  $570\text{ cm}^{-1}$  (Fig. 4d). The fine-grained feldspar and quartz aggregates show curved yet sharp boundaries to the neighboring grains. Planar shock effects can be present within adjacent quartz at the immediate contact with fine-grained feldspar aggregates (Fig. 2h). Adjacent amphibole shows cataclasis and alteration (Fig. 4a, b). These microstructures occur in both drill cores at all depths [V2 4.2 (33 cm), V2 66.4 (770 cm), V2 69.1 (809 cm), V2 71.f (861 cm), V2 78.2 (1003 cm), V3 2.1 (5 cm), V3 60.5 (659 cm), V3 66.12

(769 cm), V3 67.3 (805 cm), and V3 73.4 (994 cm)]. No polyminerally pseudotachylitic breccias, as described elsewhere from the Vredefort Dome (e.g., Killick and Reimold 1990; Dressler and Reimold 2004; Reimold and Gibson 2005, 2006; Mohr-Westheide and Reimold 2010; Reimold et al. 2016), were observed in our samples.

### Ilmenite and magnetite microfabrics

Coarse ilmenite grains can include a few tens of  $\mu\text{m}$  wide single magnetite layers, representing sandwich structures (Haggerty 1991), as well as fine-lamellar or spheroidal-shaped magnetite exsolutions of a few  $\mu\text{m}$  (Fig. 5a, b). Ilmenite and magnetite-filled veins emanating from the phase boundary of the host Fe-oxide phase into adjacent feldspar or quartz are  $\mu\text{m}$ - to tens of  $\mu\text{m}$  wide and become narrower with distance from the boundary (Fig. 5a–d). In the wider veins, magnetite typically shows straighter boundaries compared to ilmenite, which exhibits rather smoothly curved phase boundaries (Fig. 5d).

Coarser ilmenite is commonly twinned. A few  $\mu\text{m}$  to 50  $\mu\text{m}$ -wide irregular lamellar twins are characterized by boundaries parallel to  $\{\bar{1}012\}$ , a rotation axis parallel to  $\langle 02\bar{2}1 \rangle$ , and a rotation angle of  $86^\circ$  (black lines in Figs. 6a, 8a). Two different sets of  $\{\bar{1}012\}$  twins are observed. Very straight and fine-lamellar twins with boundaries parallel to  $\{10\bar{1}1\}$  crosscut the  $\{\bar{1}012\}$  twins. They are characterized by a rotation of approximately  $69^\circ$  about the  $\langle 1\bar{1}0\bar{1} \rangle$  axis, show a small spacing of  $\approx 20\text{ }\mu\text{m}$ , and a width of only few  $\mu\text{m}$  (red lines in Fig. 6a). The  $\{10\bar{1}1\}$  twins crosscut the  $\{\bar{1}012\}$  twins with marked shear offset (Fig. 6a).

Fine-lamellar magnetite exsolutions within ilmenite can occur parallel to other symmetrically equivalent  $\{10\bar{1}1\}$  planes. They have a spacing of several  $\mu\text{m}$ , a width of  $\approx 1\text{ }\mu\text{m}$ , and a length of  $\approx 5\text{ }\mu\text{m}$  (Figs. 5a, 6a, 7a, b). EBSD measurements show an epitaxial relationship, where  $\{110\}$  of magnetite is parallel to  $\{10\bar{1}0\}$  of the host ilmenite and (0001) of ilmenite coincides with  $\{111\}$  of magnetite (Fig. 7b, d, e). Crystallographically-controlled magnetite exsolution lamellae show minor relative misorientation (misorientation angles  $< 5^\circ$ ) (Fig. 7b). In contrast, the crystallographic orientation of exsolved spheroidal magnetite ( $\approx 10\text{ }\mu\text{m}$  diameter) is not controlled by the crystallographic orientation of the host ilmenite (Fig. 7a, c, e). These spheroidal magnetite exsolutions occur preferentially along the  $\{10\bar{1}1\}$  twin boundaries and along grain boundaries (Fig. 7a).

An ilmenite grain with an internal misorientation of up to  $30^\circ$  was observed to host another type of twin with a width of  $\approx 15\text{ }\mu\text{m}$  (Fig. 8a, c). This (0001) twin is characterized by a rotation axis parallel to the  $c$ -axis and a misorientation angle of  $178^\circ$  (white line [e] in Fig. 8a). Within the adjacent quartz grain, a shear fracture, which is decorated

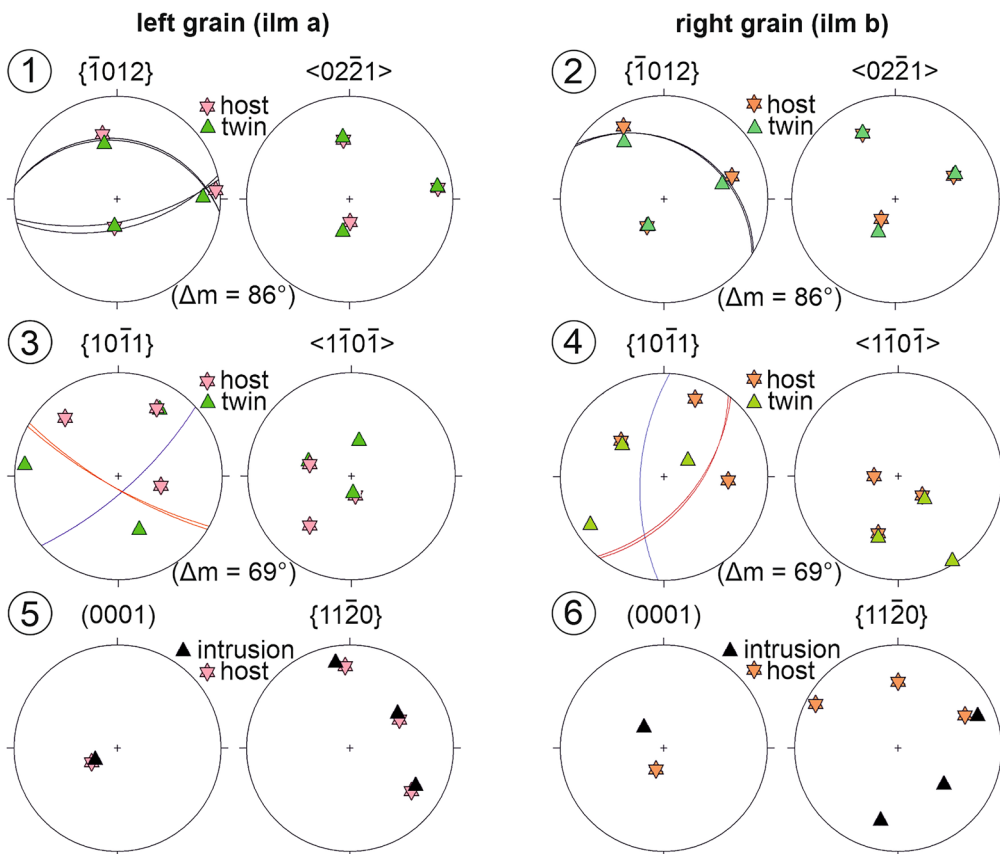
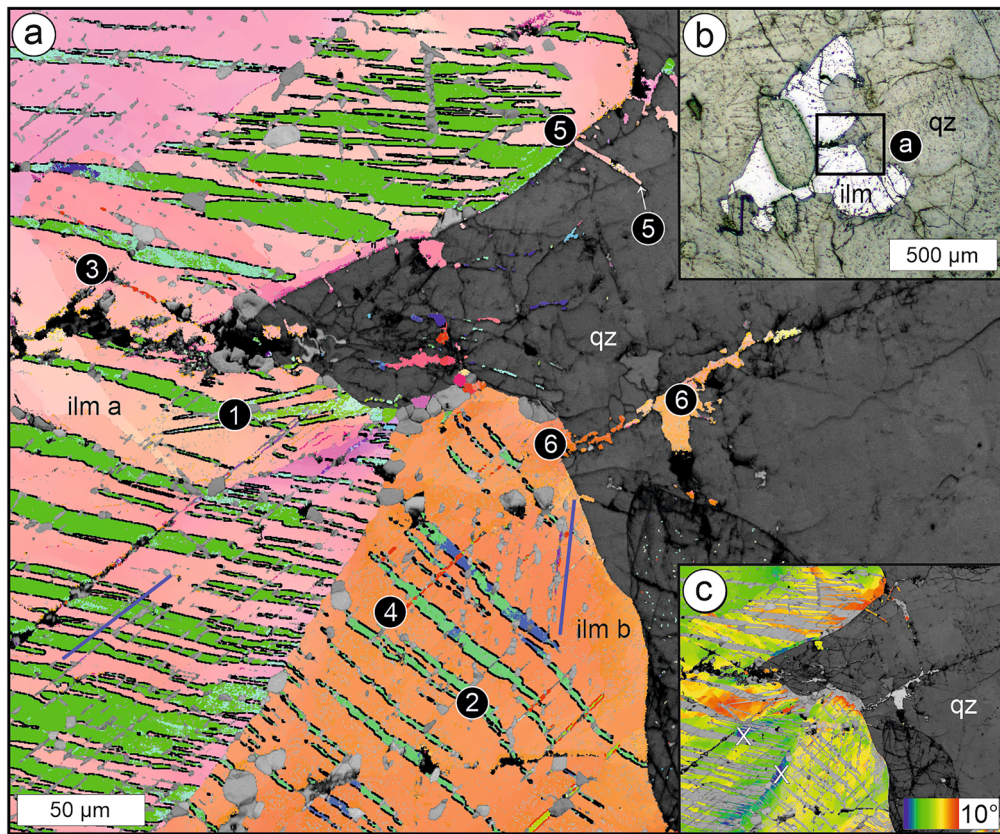




**Fig. 6** EBSD data of deformed ilmenite (sample V2 4.2, 33 cm depth). **a** Orientation map (inverse pole figure of  $z$ -direction) of two grains (ilm a and ilm b), where two different twins (red  $\{10\bar{1}2\}$  twin boundaries and black  $\{10\bar{1}1\}$  twin boundaries) are identified. The numbers correspond to the respective pole figures. Note that ilmenite along PFs of quartz (qz) has a similar orientation compared to the host. Lamellar magnetite exsolutions are oriented along  $\{10\bar{1}1\}$  planes of the ilmenite host (blue lines) plotted in **3** and **4**. **b** Reflected light photomicrograph of the ilmenite (ilm) and quartz (qz) grain partially displayed in **a**. **c** Relative misorientation angle ( $10^\circ$ ) maps for the two grains with their misorientation reference points marked by white Xs. **1, 2** Stereographic projections (lower hemisphere) of the  $\{10\bar{1}2\}$  twins with rotation axes and misorientation angle ( $\Delta m$ ). The great circles depict the orientation of the twin planes marked black in **a**. **3, 4** Stereographic projections (lower hemisphere) of the  $\{10\bar{1}1\}$  twins with rotation axes and misorientation angle ( $\Delta m$ ). The great circle depicts the orientation of the twin planes marked red and blue in **a**. **5, 6** Stereographic projections (lower hemisphere) of the (0001) and the  $\{11\bar{2}0\}$  planes of the ilmenite host and intrusion of ilm a (**5**) and ilm b (**6**) into quartz fractures depicted in **a**

by fine-grained ilmenite, is emanating in contact with the (0001) twin in the host ilmenite (compare Fig. 8a, h).

Crystallographic orientations of ilmenite filling single fractures in quartz are remarkably similar to those of the coarse adjacent ilmenite grains with misorientation angles  $\leq 10^\circ$  (Figs. 5, 6a). Magnetite along single fractures exhibits relatively homogenous crystallographic orientations (Figs. 8f, h, 9b, d). However, a systematic relationship between the crystallographic orientations of magnetite in different fractures within the same quartz grain is not apparent (Fig. 9). No crystallographic relationship with the host quartz grain was observed. The fractures in quartz are commonly parallel to Dauphiné twin boundaries, characterized by a misorientation with a rotation of  $60^\circ$  around the  $c$ -axis (Fig. 8g, i).

Coarse-grained ilmenite in samples V2 1.f (6 cm), V2 66.4 (770 cm), V3 2.1 (5 cm), V3 3.6 (15 cm), V3 3.16 (26 cm), and V3 46.1 (549 cm) is altered when in direct contact to partly chloritized biotite (Fig. 10a, d). Alteration products are anatase inclusions of a few tens of  $\mu\text{m}$  in diameter (Fig. 10b, d), as identified by Raman spectroscopy. Chlorite commonly occurs along the magnetite exsolution lamellae within the host ilmenite grains, indicating that chlorite preferentially replaces magnetite (Fig. 10c, e). Calcite occurs within the alteration products together with anatase, chlorite, and residual ilmenite (Fig. 10d, f). Within the alteration products, magnetite grains with diameters of up to  $15 \mu\text{m}$  can be identified, which have smoothly curved grain boundaries compared to the irregular grain boundaries of ilmenite and anatase (Fig. 10f).

## Discussion

Figure 11 summarizes the distribution of the observed microfabrics in the samples from the two drill cores as a function of depth. Here, we first discuss the shock conditions implied by the microstructures, then the deformation, and transformation processes of ilmenite and magnetite during impact cratering and finally the implications for rock magnetism. A summary of the observed shock effects is given in Table 1.

### Deformation conditions

The PFs in quartz are dominantly parallel to (0001) and  $\{10\bar{1}1\}$  (Figs. 2c, e, h, 3a–c, 8g, i, 9a), which are known quartz cleavage planes (e.g., Tröger 1982) and common, albeit non-diagnostic, shock effects that represent tensile cracking (Stöffler and Langenhorst 1994; French and Koberl 2010; Stöffler et al. 2018). Shearing is indicated by abundant shear fractures with shear offset, especially along the central fracture of FFs (Fig. 2c). Based on the spacing and the intrusion of Fe-phases, we interpret most of the planar features observed here as PFs. At lithologically equivalent locations at Vredefort, basal PDFs, i.e., Brazil twins parallel to (0001), were observed by transmission electron microscopy (TEM, Leroux et al. 1994). Some fine-lamellar (0001) planar features observed in our study (Figs. 2e, h, 3a, b) might represent basal PDFs. However, we did not perform TEM measurements, which would be required to resolve their nature as Brazil twins.

Only about 20% of the PFs are decorated by secondary quartz grains aligned along (0001) and  $\{10\bar{1}1\}$  cleavage planes, yet not along other rhombohedral planes, such as  $\{10\bar{1}3\}$  and  $\{10\bar{1}2\}$ , typical of PDFs that indicate higher shock pressures (Langenhorst and Deutsch 1994). Generally, we observed no microstructural evidence for rhombohedral PDFs, consistent with the findings that PFs and FFs develop at lower shock conditions. However, in association with fine-grained feldspar zones, adjacent quartz can be replaced by up to 50% with secondary quartz (Fig. 4), which might reflect local higher strain, i.e., higher shock conditions consistent with heterogeneous shock conditions on the grain scale (e.g., Gibson and Reimold 2005). Huffman et al. (1993) and Huffman and Reimold (1996) suggested that generally fewer PDFs might have been generated at Vredefort given the deep crustal levels with higher ambient temperature and pressure conditions.

Monomineralic fine-grained quartz aggregates that replace original grains, as observed in our samples, were previously described from similar locations (e.g., Schreyer and Medenbach 1981; Fricke et al. 1990; Grieve et al. 1990; Gibson and Reimold, 2005). However, no larger

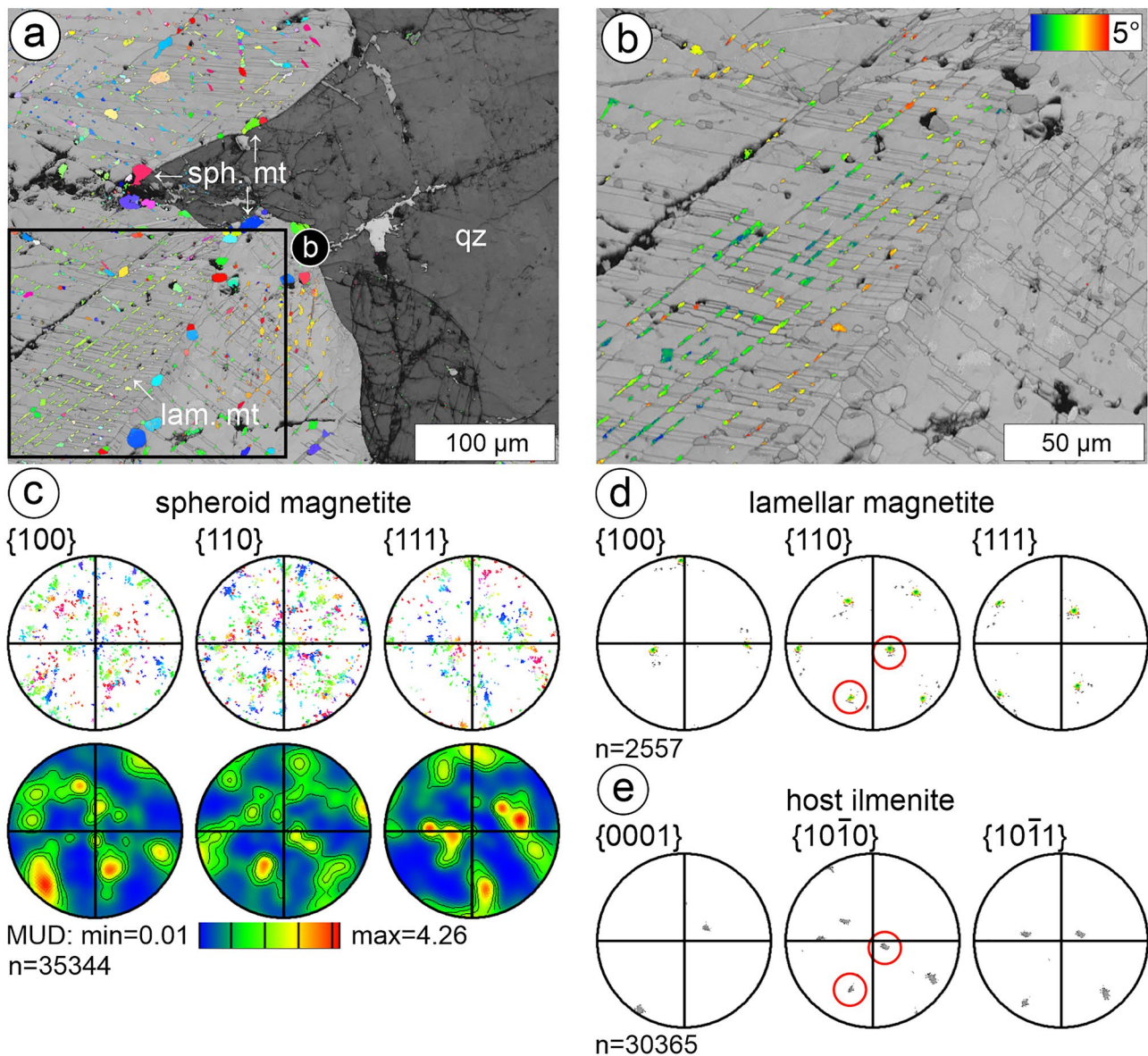


**Fig. 7** EBSD data of sample V2 4.2 (33 cm depth). **a** Two different types of magnetite grains within the ilmenite host adjacent to quartz (qz). Magnetite grains display a spheroid (sph. mt) and a lamellar (lam. mt) shape. The black rectangle marks the area magnified in **b**. **b** Misorientation map of lamellar magnetite grains (color). **c** Pole figures and density plots of the {100}, {110}, and {111} planes/axes of the spheroid magnetite grains in stereographic projections of the lower hemisphere, corresponding to the orientation map in **a**. **d** Pole figures of the {100}, {110}, and {111} planes/axes of the lamellar

magnetite grains in stereographic projections of the lower hemisphere, corresponding to the orientation map in **b**. The red circles indicate the epitactic relationship with the ilmenite host orientation displayed in **e**. **e** Pole figures of the {0001}, {10 $\bar{1}$ 0}, and {10 $\bar{1}$ 1} planes of the host ilmenite in stereographic projections of the lower hemisphere, corresponding to the orientation map in **b**. The red circles indicate the epitactic control of the lamellar magnetite orientation displayed in **d**

scale pseudotachylitic breccias with polymineralic lithic components documented elsewhere in the Vredefort dome (e.g., Killick and Reimold 1990; Dressler and Reimold 2004; Reimold and Gibson 2005, 2006; Mohr-Westheide and Reimold 2010; Reimold et al. 2016) are present in our samples. Nor did we find high-pressure SiO<sub>2</sub> polymorphs as described in samples within the Witwatersrand quartzites

surrounding the Vredefort Dome (e.g., Martini et al. 1978, 1991, 1992). The new quartz grains are aligned parallel to crystallographic planes, which are known quartz cleavage planes with crystallographic orientations similar to that of the host grain (Fig. 3a). This suggests that the newly created quartz formed by effective strain-induced grain boundary migration, i.e., recrystallization, along the damage zone of



the cracks during static annealing without the involvement of a melt or a glass being necessary. Formation of new grains with a similar microstructure was described in high strain-rate deformation experiments with subsequent annealing (“kick-and-cook” experiments of Trepmann et al. 2007), i.e., strings of quartz grains generated along the damage zone of pre-existing cracks with a crystallographic orientation controlled by the host quartz crystal. However, the involvement of glass or melt cannot be ruled out given the prolonged post-impact thermal history of the Vredefort gneisses. This is especially true for the fine-grained aggregates replacing pre-impact quartz grains in the center (Fig. 4b), which are found only spatially related to fine-grained feldspar aggregates with K-feldspar-plagioclase schlieren (Figs. 2h, 4). The fine-grained feldspar aggregates suggest some mobility, indicating either localized stronger cataclasis or even “monomineralic” melting of feldspar, consistent with the lower melting temperature and fracture toughness of feldspar compared to quartz (Spray 2010, Fig. 12). Therefore, the fine-grained quartz and feldspar microstructures defining few  $\mu\text{m}$  to hundreds of  $\mu\text{m}$ -wide, mm-long zones (Figs. 2h, 4), indicate that they represent localized higher strain compared to the host rock. This strain localization may be due to deformation after the passage of the shock wave during the modification stage of impact cratering (then these microstructures might represent cataclasites or potentially pseudotachylytes, that involve frictional melts) or due to deformation at high shock conditions related to the shock wave through the mechanical contrast between feldspar and quartz (hence, these microstructures might be called “shock veins” that potentially involve shock melting). However, it is impossible from our observed microstructures alone, and lies outside the scope of our study, to distinguish the two. For a recent review on the ongoing discussion of shock melting versus frictional melting, the reader is referred to Spray and Biren (2021) and references therein. We, therefore, use the term “shear zones” in the sense that the microstructures observed here represent localized zones of increased strain given the higher number of fine-grained aggregates when compared to the host rock.

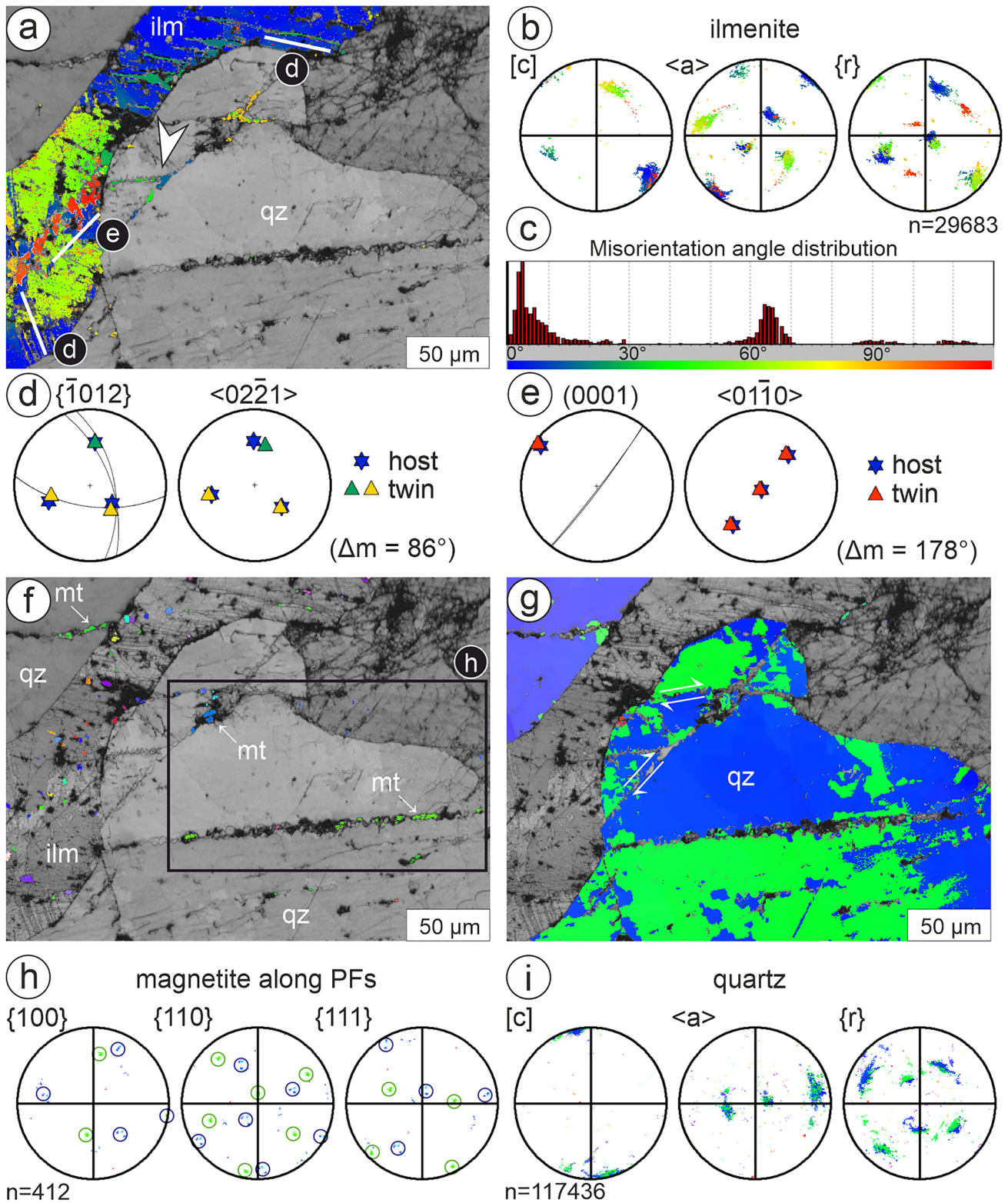
The observed shock effects of biotite kink bands (see Fig. 2a, g), PFs and FFs, possible basal PDFs in quartz that are partly decorated by recrystallized grains, and the absence of evidence for rhombohedral PDFs in quartz, together suggest our samples experienced F-S2 to F-S3 shock stages (Stöffler et al. 2018) and between 0 and Ia shock stages according to the IUGS system (Stöffler and Grieve 2007). FFs have been reported to occur at shock pressures up to 18 GPa (Tada et al. 2022). Given the lack of annealed rhombohedral PDFs in our samples on one hand, and considering the general difficulty of constraining shock pressure, not to mention its heterogeneous character, in addition to the strong modification due to the prolonged thermal history after the

impact, we conclude that shock conditions were  $< 20$  GPa. This shock level is consistent with the observations from samples at similar positions in the Vredefort impact structure (e.g., Grieve et al. 1990; Reimold and Gibson 2005). At these relatively low shock conditions, shock-related shear deformation might be expected (Trepmann 2008; Ebert et al. 2020), which is consistent with the potential presence of (0001) Brazil twins and the abundance of shear fractures.

The fact that the Dauphiné twin boundaries lie parallel to the PFs (Fig. 8h) implies they were generated after impact, when the fracture surfaces served as preferred sites of twin nucleation, as observed at the Charlevoix impact structure (Trepmann and Spray 2005). Dauphiné twins can occur from the transformation of hexagonal  $\beta$ -quartz to trigonal  $\alpha$ -quartz, when cooled below the transition temperature of  $\approx 573$  °C at atmospheric pressure (Tullis 1970; Markgraaff 1986; Heaney and Veblen 1991) or  $\approx 25$  °C/kbar under elevated confining pressure (Coe and Paterson 1969). Assuming a structural uplift of 3–12 km and an erosion of 8–11 km since then (Gibson et al. 1998, 2019) and a geothermal gradient of 30 °C/km (Gibson and Wallmach 1995) in combination with a rock density of 2700 kg/m<sup>3</sup>, a temperature of about 650–725 °C would be required for stabilizing  $\beta$ -quartz. Thus, if the observed Dauphiné twins formed during cooling from  $\beta$ -quartz to trigonal  $\alpha$ -quartz stability conditions, the rocks were at temperatures above 650–725 °C during impact cratering. These temperatures appear quite realistic, given the high post-shock temperatures estimated to about 650–750 °C based on petrological constraints inferred from reaction fabrics (orthopyroxene-plagioclase coronas and cordierite-orthopyroxene symplectites) in metapelites of the Archean basement, which were interpreted to have formed after the impact (Perchuk et al. 2002).

### Shear heating and mobilization of ilmenite and magnetite

Several studies have observed opaque minerals in shock-induced planar features in the Vredefort gneisses (Hart et al. 1991, 2000; Cloete et al. 1999; Carporzen et al. 2006). Cloete et al. (1999) suggested that they formed by crystallization from a melt. Moreover, Cloete et al. (1999) found that magnetite crystallized with its  $\langle 101 \rangle$  sub-parallel to  $\{ \bar{1} 100 \}$  of the host quartz grains as well as magnetite sub-parallel to an orientation of  $\langle 101 \rangle$  on the sample scale. Our observations also show a remarkably homogeneous crystallographic orientation of magnetite, but only within single fractures, with no sub-parallel relationship of  $\langle 101 \rangle$ , with no control of  $\{ \bar{1} 100 \}$  from the host quartz and independent of the magnetite in other fractures within the same host quartz grain (Figs 8f–i, 9). The crystallographic orientation of ilmenite within PFs of quartz seems to be controlled by the host ilmenite orientation from which the veins emanate,



and not by the crystallographic orientation of the silicate phase (Figs. 6a, 8a). We suggest that shear heating during shock-related deformation at non-isostatic stresses of both the host Fe-phase and the adjacent silicates (Fig. 8a, g)

played a major role in mobilizing ilmenite and magnetite, as well as chalcopyrite and pyrite, to intrude shear fractures within quartz and feldspar. Depending on the composition and eutectic temperature, shear heating can partially or



**Fig. 8** EBSD data of sample V3 2.1 (5 cm depth). **a** Misorientation map of an ilmenite grain (ilm) with two different twins (white lines) corresponding to **d** and **e** as well as associated ilmenite (white arrow) within PFs of quartz (qz). Note that the localized zone of increased misorientation in ilmenite related to the (0001) twin (red) is spatially related to shear fractures within the adjacent quartz, which are decorated by ilmenite. **b** Pole figures of the *c*-plane, as well as the *a*- and *r*-axes of ilmenite in stereographic projections of the lower hemisphere, corresponding (colored) to the misorientation map in **a**. **c** Misorientation angle distribution of the misorientation map in **a**. **d, e** Stereographic projections (lower hemisphere) of the  $\{10\bar{1}2\}$  and (0001) twins with rotation axes and misorientation angle ( $\Delta m$ ). The great circles depict the orientation of the twin planes marked white in **a**. **f** EBSD orientation map (inverse pole figure of *z*-direction) of magnetite (mt) within an ilmenite grain (ilm) and within PFs of quartz (qz). The black rectangle indicates the data area of **h**. **g** EBSD orientation map (inverse pole figure of *z*-direction) of a quartz grain (qz) displaying a Dauphiné twin relationship (blue and green) as well as shear offsets (white double arrows) along PFs. **h** Pole figures of the  $\{100\}$ ,  $\{110\}$ , and  $\{111\}$  planes/axes of magnetite along PFs of quartz in stereographic projections of the lower hemisphere, corresponding to the orientation map in **f**. **i** Pole figures of the *c*-plane, as well as the *a*- and *r*-axes of quartz in stereographic projections of the lower hemisphere, corresponding to the orientation map in **g**

completely melt/breakdown chalcopyrite, pyrite, ilmenite, and magnetite (Nakamura et al. 2002) and thus strongly influence their mobility. Opaque minerals have not been observed along phase or grain boundaries, but exclusively along PFs in quartz commonly associated with shear offsets (Figs. 2c, d, 8) as well as along shear fractures within feldspar. The crystallographic continuity with the source Fe-bearing phase might be explained by epitactic crystallization in the vein, where the host phase acted as a substrate that dictated the crystallographic orientation of the newly precipitated phase.

The two main controlling factors of frictional melting are the melting point/breakdown temperature ( $T_{MB}$ ) of the respective phases as well as their fracture toughness ( $K$ ) (Fig. 12) (Spray 1992, 2010). In relation to their melting point and fracture toughness, Spray (2010) suggested a hierarchy in the response to comminution (grain size reduction) and frictional melting of minerals. Feldspar, pyrite, magnetite, and quartz show increasing values of fracture toughness and melting/breakdown temperatures (Fig. 12), which leads to a decreasing tendency of the respective phases to fracture or melt. Those mechanical properties appear to correlate with the microstructures of pyrite (Figs. 2d, 9b) and magnetite (Figs. 2d, 5, 8f, 9b) along the fractures in quartz and feldspar. Magnetite has the highest fracture toughness and melting temperature among the iron-bearing phases

and preferentially displays brittle fracturing. Ilmenite, on the other hand, displays smoothly curved phase boundaries (Fig. 5) and, in general, appears more often within fractures of adjacent silicate phases. Therefore, its mobility might be explained by the lower melting point (Eriksson and Pelton 1993) in combination with a lower fracture toughness in relation to magnetite.

### Ilmenite twinning

Twins parallel to  $\{10\bar{1}2\}$  are common in ilmenite (Minkin and Chao 1971; Frick 1973; Reynolds 1984). The tens of  $\mu\text{m}$  wide  $\{10\bar{1}2\}$  twins with irregular boundaries indicate that they were modified by twin boundary migration. We, therefore, interpret them as pre-shock deformation structures. The fine-lamellar  $\{10\bar{1}1\}$  twins offset and thus postdate the  $\{10\bar{1}2\}$  twins (Fig. 6). They show very straight boundaries and can be wedge-shaped, indicating that they are mechanical twins. Mechanical twinning is a crystal-plastic deformation mechanism at non-isostatic stresses, involving dislocation glide, which does not require diffusion and is thus fast and not thermally controlled. The (0001) single twin, which shows irregular boundaries, is related to a site of high strain as indicated by misorientation angles and spatially related to shear fractures decorated by ilmenite in the adjacent quartz (Fig. 8). Deformation-induced  $\{10\bar{1}1\}$  twins have been reported in natural samples and from experiments at confining pressures of 1.3 GPa with applied differential stress of 0.75 GPa and a strain rate of  $10^{-4}/\text{s}$  at 25 °C (Minkin and Chao 1971). Twin planes parallel  $\{10\bar{1}1\}$  and (0001) in ilmenite were reported from shock experiments as well as in ilmenite from lunar rocks (Minkin and Chao 1971; Sclar et al. 1973). Therefore, we interpret the  $\{10\bar{1}1\}$  and (0001) twins to be related to the high strain rate deformation at non-isostatic stress conditions related to meteorite impacting, consistent with the quartz and feldspar microstructures.

### Exsolution of magnetite within ilmenite

In contrast to twinning, exsolution requires diffusion. The magnetite exsolution lamellae, as well as the twins parallel to  $\{10\bar{1}1\}$  planes of ilmenite, crosscut and offset the  $\{10\bar{1}2\}$  twins (Fig. 6a) and thus postdate the  $\{10\bar{1}2\}$  twins. Exsolved magnetite in ilmenite occurred during subsolidus re-equilibration from slow cooling (Buddington and Lindsley 1964;

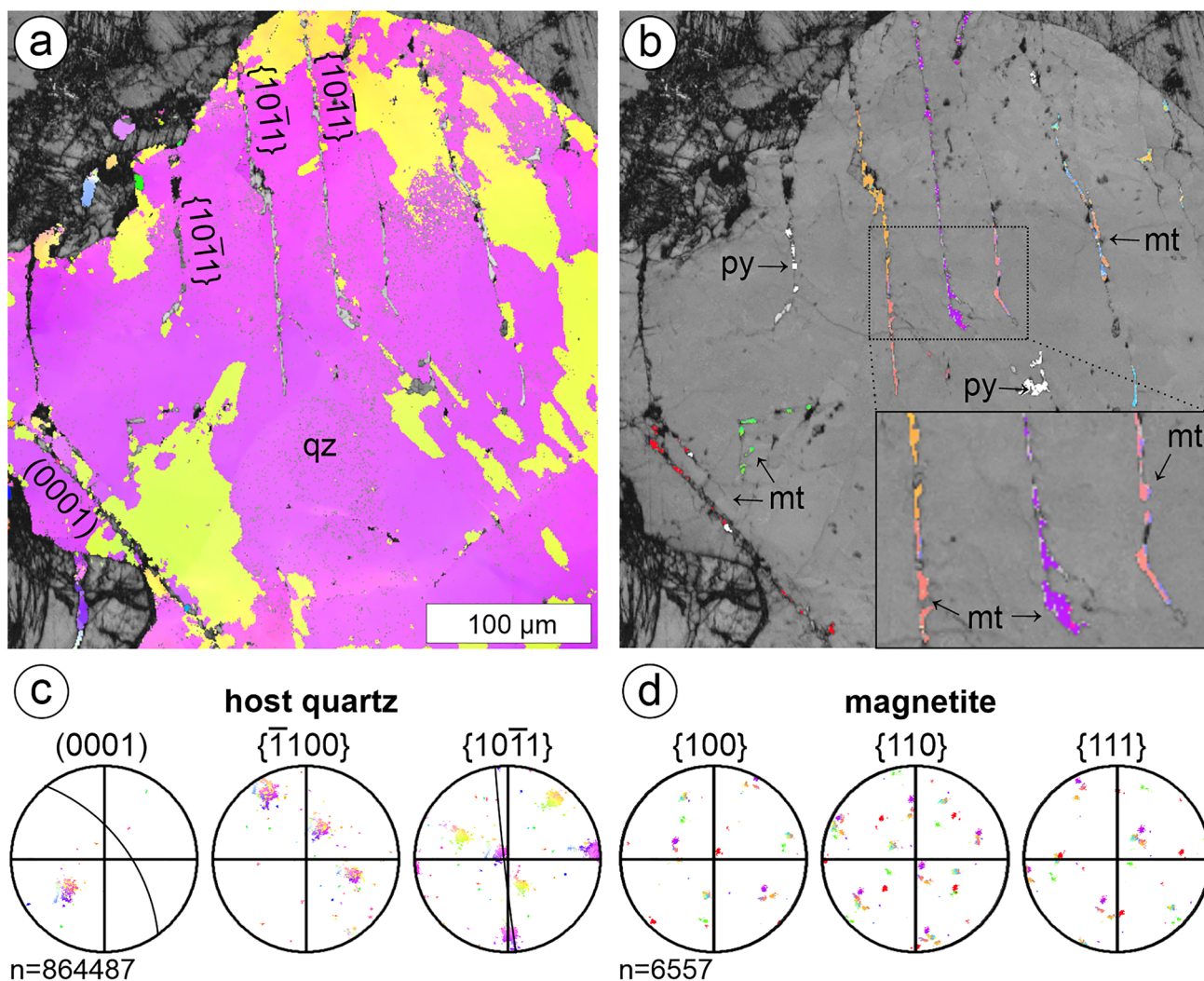


**Fig. 9** EBSD and U-stage data of sample V3 34.12 (384 cm depth). **a** EBSD orientation map (inverse pole figure of  $z$ -direction) of a quartz grain (qz) displaying Dauphiné twins (yellow and violet) as well as PFs oriented along (0001) and  $\{10\bar{1}1\}$ . **b** EBSD orientation map (inverse pole figure of  $z$ -direction) of magnetite (mt) along PFs of quartz (qz). Note that magnetite shows distinct orientations in the different PFs. The occurrence of pyrite is indicated in white. **c** Pole

figures of (0001),  $\{\bar{1}100\}$ , and  $\{10\bar{1}1\}$  with PF great circles of the host quartz in stereographic projections of the lower hemisphere, corresponding to the orientation map in **a**. **d** Pole figures of  $\{100\}$ ,  $\{110\}$ , and  $\{111\}$  of magnetite along PFs of quartz in stereographic projections of the lower hemisphere, corresponding to the orientation map in **b**

Tan et al. 2016). It has also been described to form during cooling after meteorite shock events (Sclar et al. 1973). The temperatures required to exsolve magnetite from ilmenite must have been higher than the ilmenite–hematite miscibility gap at 600–700 °C; otherwise, hematite would be expected to have formed (Lindsley 1991; Harrison 2000).

Epitactic relations of magnetite exsolution in ilmenite are related to the densely packed oxygen planes of magnetite and ilmenite (Wenk et al. 2011; Tan et al. 2016). We observed an epitactic relation only for those magnetite exsolution lamellae that were controlled in shape and occurrence by the ilmenite  $\{10\bar{1}1\}$  planes (Fig. 7b, d, e). There, the

magnetite  $\{110\}$  planes parallel the  $\{10\bar{1}0\}$  planes of the host ilmenite (Fig. 7d, e). In contrast, spheroidal magnetite exsolution show neither shape nor crystallographic orientation that are controlled by the crystallography of the ilmenite host. However, the spheroidal magnetite exsolution occur preferentially along the  $\{10\bar{1}1\}$  twins and grain boundaries, indicating heterogeneous nucleation at sites of increased disorder that facilitated diffusion. The magnetite exsolution lamellae in ilmenite crosscut the pre-shock  $\{10\bar{1}2\}$  twins and are associated with the fine-lamellar  $\{10\bar{1}1\}$  twins that are interpreted as having been shock-induced. Therefore,



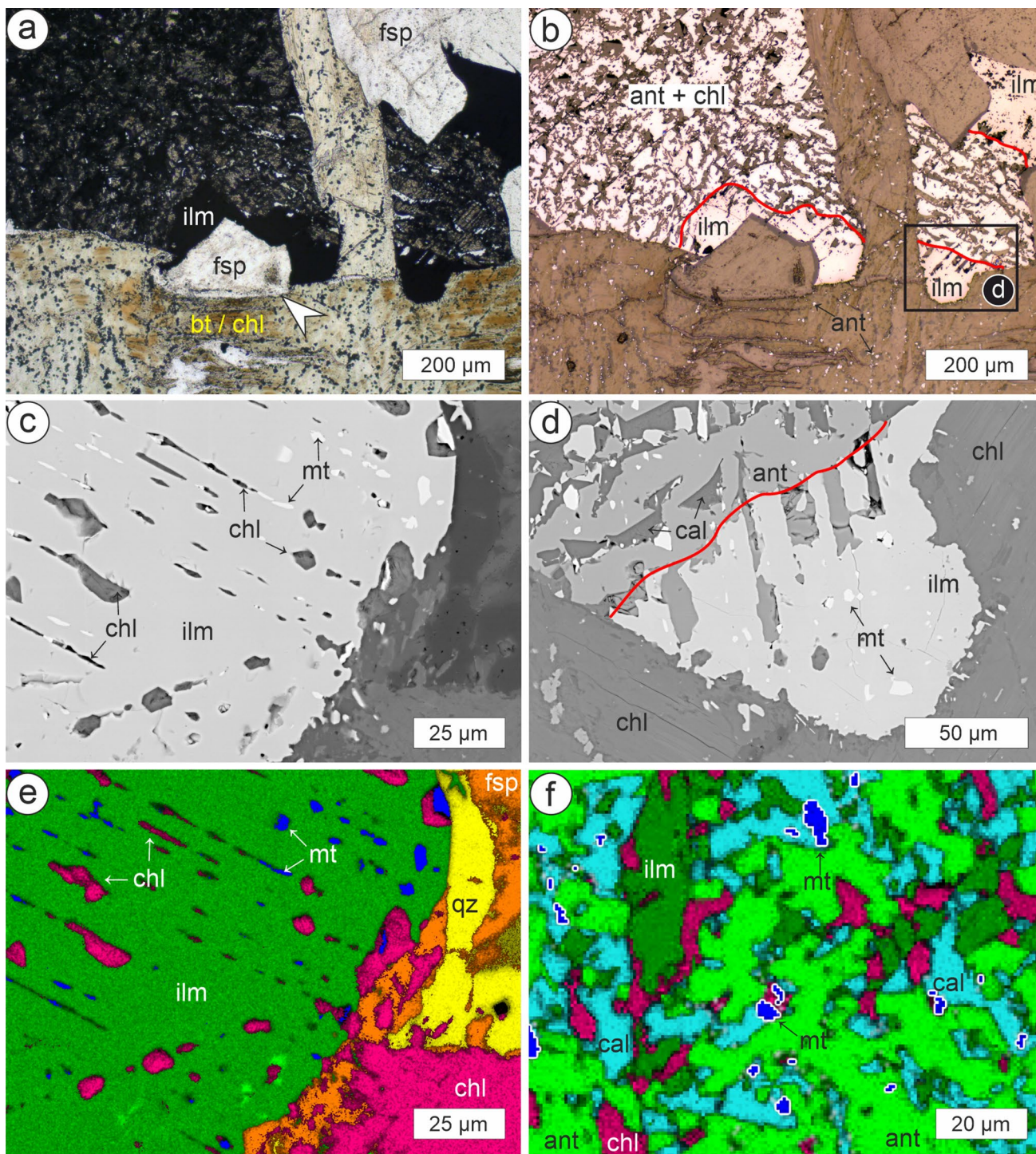


**Fig. 10** Altered ilmenite. **a, b** Altered ilmenite in direct contact with chloritized biotite (bt/chl) and feldspar (fsp). The alteration fronts are displayed by red lines and separate the alteration products consisting of anatase and chlorite (ant+chl) from the residual ilmenite (ilm). Note the feldspar grain (white arrow) in between an ilmenite and a chloritized biotite. Few  $\mu\text{m}$ -sized anatase grains also occur within biotite/chlorite. The black rectangle indicates the image of **d**. Image **a** taken with transmitted light and image **b** taken with reflected light. **c** Magnetite exsolution (mt) within the host ilmenite (ilm) replaced by

chlorite (chl). BSE image. **d** Altered ilmenite, where residual ilmenite (ilm) with magnetite exsolution (mt) occurs in direct contact with chlorite (chl), which locally reacted to anatase (ant). Calcite (cal) is also observed. The red line displays the alteration front. BSE image. **e** Phase map based on EDS data displaying image section of **c** with ilmenite (ilm), magnetite (mt), chlorite (chl), biotite (bt), and quartz (qz). **f** Phase map based on EDS data showing a reaction microfabric of altered ilmenite consisting now of anatase (ant), calcite (cal), chlorite (chl), and magnetite (mt)

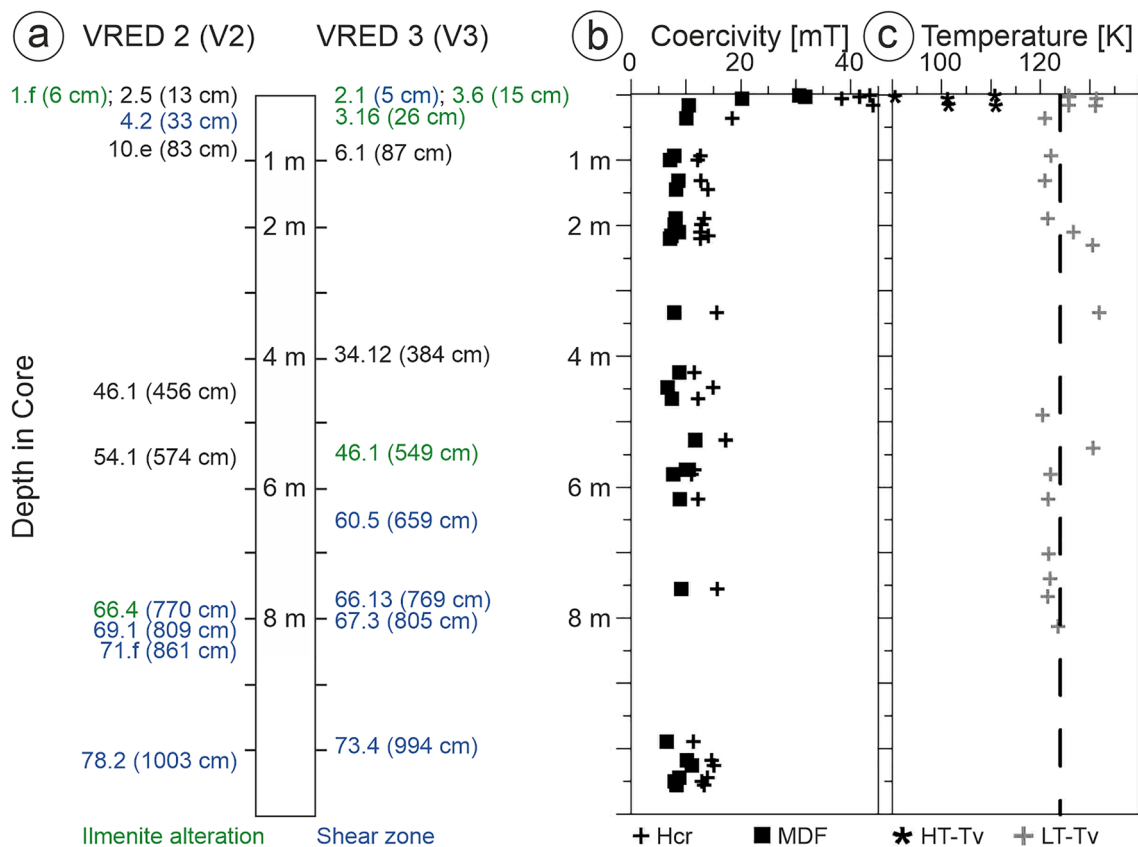


**Fig. 11** Summary of microstructural observations of samples from the VRED2 (V2) and VRED3 (V3) drill cores versus magnetic properties reported for the same material by Carporzen et al. (2012). Fe-phase-bearing veins in shear fractured feldspar and quartz occur at all depths. **a** Samples of drill cores V2 and V3 displaying ilmenite alterations (green) and shear zones (blue). Note that samples V2 66.4 and V3 2.1 contain both ilmenite alterations and shear zones. **b** Remanent

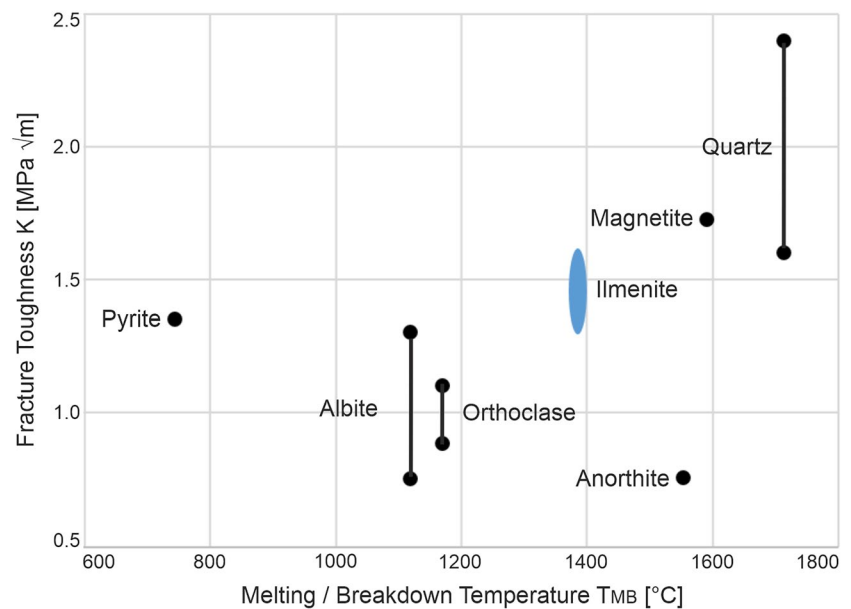
coercivity  $H_{cr}$  and median demagnetizing field (MDF) summarized for both drill cores. Datapoints in black adopted from Carporzen et al. (2012). **c** High- and low-temperature Verwey transitions (HT-Tv; LT-Tv) summarized for both drill cores. Vertical dashed line at 124 K displays the Verwey transition temperature for pure stoichiometric magnetite. **b, c** after Carporzen et al. (2012)

**Table 1** Summary of the observed shock effects in different components

Mineral	Shock effect	Figure references
Ilmenite	{101̄1}/(0001) twin	Figs. 6, 8a–c
	µm-scale veins along PFs and FFs within quartz and shear fractures in feldspar	Figs. 5, 6, 8a
	Alteration to anatase, chlorite, calcite, and magnetite	Figs. 10, 11
Magnetite	Lamellar and spheroid exsolutions within coarse ilmenite	Figs. 5a, b, 7, 10c–e
	µm-scale intrusions PFs within quartz and fractures within feldspar	Figs. 2d, 5, 8f, 9b
Quartz	PFs/FFs	Figs. 2c,e,h, 3a–c
	Dauphiné twin	Figs. 8g, 9a
	Partially recrystallized	Fig. 3
Biotite	Kink bands	Fig. 2a, g
Pyrite/Chalcopyrite	µm-scale intrusions in PFs of quartz and fractures of feldspar	Figs. 2d, 9b
Feldspar	Fine-grained schlieren structure associated with recrystallized quartz in shear zones	Figs. 2h, 4, 11



**Fig. 12** Melting/breakdown temperature  $T_{MB}$  of selected mineral phases with their respective fracture toughness  $K$  (Rankin 1915; Morey and Bowen 1922; Shimada 1969; Eriksson and Pelton 1993; Galwey and Brown 1999; Tromans and Meech 2002; Broz et al. 2006; Whitney et al. 2007; Spray 2010; Deer et al. 2013). The fracture toughness of chalcopyrite and ilmenite (blue) was roughly estimated by the authors based on the observations of the investigated microfabrics of this study



the magnetite within the lamellae likely crystallized during cooling after impact.

### Ilmenite alteration

Samples V2 1.f (6 cm), V2 66.4 (770 cm), V3 2.1 (5 cm), V3 3.6 (15 cm), V3 3.16 (26 cm), and V3 46.1 (549 cm) contain altered ilmenite and magnetite. Chlorite is formed at the expense of biotite and magnetite; ilmenite is partially transformed into the Ti-phase anatase. Chloritized biotite throughout the drill core often contains a few  $\mu\text{m}$ -sized anatase grains (Fig. 10b, d, f), which might represent alteration products. Ilmenite can be largely replaced by a mineral assemblage of anatase, chlorite, calcite, ilmenite, and small magnetite grains—the latter occur primarily in contact with calcite, chlorite, and anatase. The observation that magnetite exsolutions within an ilmenite host are only replaced by chlorite when in direct contact with altered biotite (Fig. 10a–d), but not in contact with feldspar, indicates that fluid availability, and hence alteration, depended on being in direct contact with water-bearing minerals.

### Implications for magnetic properties

An important starting point of this study was to disentangle Fe-oxide microstructures that are related to shock effects from the meteorite impact event from those that might have been related to lightning. We did not find evidence for lightning-generated microstructures in the uppermost meter of either core. Carporzen et al. (2012) suggested, based on high coercivities ( $> 30$  mT) and low Verwey transition temperatures (Fig. 11), that oxidized, SD magnetite ( $< 100$  nm) formed from the lightning strikes at the surface. However,

such small grain sizes are below the resolution of the analytical techniques we used.

Salminen et al. (2009) found that granophyre and pseudotachylitic breccia from Vredefort samples contain a few  $\mu\text{m}$ -sized and a second  $> 50$   $\mu\text{m}$ -sized altered generation of a magnetic phase with high Koenigsberger ratios. They suggested that the high Koenigsberger ratios could be related to high temperatures of the rocks that were uplifted due to the Vredefort impact. Nakamura et al. (2010) argued that Fe-oxides within chloritized biotite largely contribute to the magnetic remanence at Vredefort. Granophyre dikes or polymineralic pseudotachylitic breccia, however, are not present in our samples. Although altered biotite and ilmenite are common in our samples (V2 66.4, 770 cm and V3 46.1, 549 cm), the few  $\mu\text{m}$ -sized opaque minerals within (altered) biotite and chlorite in our samples were mostly anatase (Fig. 10b). Given the occurrence of multiple generations of magnetite at all depths in the drill core (Fig. 10), we cannot associate specific magnetite populations as principal contributors to the negative magnetic anomaly.

The temperature of the drilled samples prior to impact is an important factor to explain the magnetic remanence of the host rocks. As discussed above, the temperature of the pre-impact basement (650–725 °C) was higher than the Curie temperature of magnetite (580 °C), as already suggested by Henkel and Reimold (2002) and Salminen et al. (2009). Any additional temperature from impact (i.e., shock heating) cannot be distinguished from the thermal remanence recorded by different magnetite populations. Hence, one should not use the term shock remanent magnetization to describe the thermal remanences in the central region of the Vredefort impact structure.

Two types of magnetite exsolutions within ilmenite formed, related to preceding crystal-plastic deformation probably associated with frictional heating during impact cratering (Fig. 7b, d, e). Both the randomly oriented spheroid exsolutions as well as the crystallographically controlled lamellar exsolutions likely increase the thermal remanent magnetization of the host rock.

Fracturing of coarse magnetite leads to grain size reduction and potentially a transition from MD to SD magnetite, thereby enhancing the remanent magnetization and coercivity. As shown by Carporzen et al. (2006), locally enriched fine-grained magnetite, like that in polymineralic pseudotachylyte formed during impact cratering, can display Verwey transition temperatures ranging from 94 and 111 K. Based on our observations, both investigated drill cores contain fine-grained (albeit almost monomineralic quartz aggregates and feldspar aggregates) shear zones within the top 100 cm, and also below 6 m (Fig. 11). The occurrence of two Verwey transition temperatures within the top 100 cm might therefore arise from pre-impact coarse-grained magnetite with high Verwey transition temperatures ( $\approx 124$  K) and potentially newly formed, fine-grained magnetite with low Verwey transition temperatures (94–111 K), which, however, are below the resolution limit of the SEM as they are skewed toward SD sizes, roughly less than a few 100 nm.

It seems possible that samples collected as a function of distance from the center should reveal systematic differences in remanent magnetization. Approaching the paleosurface (i.e., toward the sediments), the pre-impact basement temperature should have been below the Curie temperature of magnetite, so the original magnetite there should have different remanence characteristics than the thermoremanent magnetization acquired around 2.02 Ga. This could explain the lack of high-amplitude negative anomalies in the amphibolite facies aureole (Fig. 1). Carporzen (2003; 2006) tried to test this, but the lightning-induced component overprinted the 2.02 Ga (or older) remanence, because the samples were collected on the surface. To observe an influence on the remanence characteristics, one should use the Winkie-drill approach (Carporzen et al. 2012) to obtain lightning-free material along a radial transect approaching the paleo-surface.

## Conclusions and summary

The studied Archean gneisses from the Vredefort impact structure reveal shock-related deformation of Fe-phases and silicates at non-isostatic stress conditions. The observed PFs and FFs in quartz, which is partially recrystallized, as well as kink bands in biotite, and the abundant shear fractures and shear zones, together with the lack of evidence

for rhombohedral PDFs, indicate that shock pressures were less than 20 GPa. Our documented impact-related shock effects in Fe-bearing minerals at these shock conditions are as follows:

1. Mechanical (0001) and  $\{10\bar{1}1\}$  twins in coarse pre-impact ilmenite indicate shock-related dislocation glide-controlled deformation (no diffusion required) at non-isostatic stresses.
2. Upon cooling after shock heating, crystallographically-controlled lamellar magnetite ( $\approx 5 \times 1 \mu\text{m}$ ) and spheroid magnetite ( $\approx 10 \mu\text{m}$ ) formed by exsolution within ilmenite. The lamellar magnetite exsolutions are parallel  $\{10\bar{1}1\}$  of the host ilmenite. The spheroidal magnetite exsolutions occur at sites of increased disorder, e.g., along grain boundaries and phase boundaries, aside from twin boundaries, that facilitated diffusion.
3. Shock-related shear deformation and resulting frictional heating of pre-impact magnetite and ilmenite resulted in mobilization of Fe-bearing phases such as ilmenite, magnetite, pyrite, and chalcopyrite, including injection into shear fractures of adjacent quartz and feldspar.
4. The crystallographic orientation of ilmenite within fractures of quartz and feldspar is controlled by an epitaxial relationship with the host ilmenite.
5. Comparing ilmenite and magnetite along shear fractures in quartz and feldspar, magnetite appears to be more effectively deformed by cataclasis, whereas pre-impact ilmenite deforms by crystal-plastic deformation (i.e., twinning, dislocation glide), consistent with the relatively higher fracture toughness and melting point of magnetite.

The implications of the magnetic properties are:

1. Impact related fracturing of coarse-grained magnetite likely increased the remanence carrying capacity of the existing MD magnetite as found in laboratory experiments (Carporzen and Gilder 2010). This, together with the newly formed fine-grained magnetite exsolutions within ilmenite, increases the remanent magnetization of the host rock and contributes to the strong, negative magnetic km-scale anomaly northwest of the impact structure's center.
2. Quartz Dauphiné twins restricted to PFs imply temperatures around 650–725 °C (given the assumed paleo-depth of 11–23 km) during impact cratering and are therefore higher than the Curie temperature of magnetite (580 °C). Therefore, the paleomagnetic remanence is best explained by impact-related uplifting of the initially hot material and cooling in the magnetic field direction present during the Vredefort impact.



3. No lightning-related microfabric or magnetic phase could be identified within the top 100 cm of the drill core, although magnetic properties suggest a strong influence. Those grains likely reside in the SD grain size range (< 100 nm) below the resolution of the SEM.

**Acknowledgements** The thoughtful and constructive reviews of Wolf Uwe Reimold and Christian Koeberl as well as the editorial handling of Timothy Grove are greatly appreciated and substantially improved the original manuscript. We acknowledge financial support from the Deutsche Forschungsgemeinschaft TR534/9-1 and GI712/20-1. We owe much gratitude to Rodger Hart and Laurent Carporzen, whose enthusiasm and tenacity facilitated the deep drilling project at Vredefort.

**Funding** Open Access funding enabled and organized by Projekt DEAL.

**Open Access** This article is licensed under a Creative Commons Attribution 4.0 International License, which permits use, sharing, adaptation, distribution and reproduction in any medium or format, as long as you give appropriate credit to the original author(s) and the source, provide a link to the Creative Commons licence, and indicate if changes were made. The images or other third party material in this article are included in the article's Creative Commons licence, unless indicated otherwise in a credit line to the material. If material is not included in the article's Creative Commons licence and your intended use is not permitted by statutory regulation or exceeds the permitted use, you will need to obtain permission directly from the copyright holder. To view a copy of this licence, visit <http://creativecommons.org/licenses/by/4.0/>.

## References

- Antoine LAG, Nicolaysen LO, Niccol SL (1990) Processed and enhanced gravity and magnetic images over the Vredefort structure and their interpretation. *Tectonophysics* 171:63–74. [https://doi.org/10.1016/0040-1951\(90\)90090-U](https://doi.org/10.1016/0040-1951(90)90090-U)
- Appel PWU, Abrahamsen N, Rasmussen TM (2006) Unusual features caused by lightning impact in West Greenland. *Geol Mag* 143:737–741. <https://doi.org/10.1017/S0016756806002391>
- Armstrong RA, Compston W, Retief EA, Williams IS, Welke HJ (1991) Zircon ion microprobe studies bearing on the age and evolution of the Witwatersrand triad. *Precambrian Res* 53:243–266. [https://doi.org/10.1016/0301-9268\(91\)90074-K](https://doi.org/10.1016/0301-9268(91)90074-K)
- Bauer M, Davydovskaya P, Janko M, Kaliwoda M, Petersen N, Gilder SA, Stark RW (2011) Raman spectroscopy of laser-induced oxidation of titanomagnetites. *J Raman Spectrosc* 42:1413–1418. <https://doi.org/10.1002/jrs.2849>
- Broz ME, Cook RF, Whitney DL (2006) Microhardness, toughness, and modulus of Mohs scale minerals. *Am Mineral* 91:135–142. <https://doi.org/10.2138/am.2006.1844>
- Buddington AF, Lindsley DH (1964) Iron-titanium oxide minerals and synthetic equivalents. *J Petrol* 5:310–357. <https://doi.org/10.1093/petrology/5.2.310>
- Carporzen L (2003) Magnétisme à très haute pression: Étude du cratère d'impact de Vredefort, Afrique du Sud, Masters Thesis, Institute de Physique du Globe de Paris
- Carporzen L (2006) Magnétisme des cratères d'impact de météorite à Vredefort (Afrique du Sud) et Rochechouart (France), PhD Dissertation, Institute de Physique du Globe de Paris
- Carporzen L, Gilder SA, Hart RJ (2005) Palaeomagnetism of the Vredefort meteorite crater and implications for craters on Mars. *Nature* 435:198–201. <https://doi.org/10.1038/nature03560>
- Carporzen L, Gilder SA (2010) Strain memory of the Verwey transition. *J Geophys Res* 115:B05103. <https://doi.org/10.1029/2009JB006813>
- Carporzen L, Gilder SA, Hart RJ (2006) Origin and implications of two Verwey transitions in the basement rocks of the Vredefort meteorite crater, South Africa. *Earth Planet Sci Lett* 251:305–317. <https://doi.org/10.1016/j.epsl.2006.09.013>
- Carporzen L, Weiss BP, Gilder SA, Pommier A, Hart RJ (2012) Lightning remagnetization of the Vredefort impact crater: no evidence for impact-generated magnetic fields. *J Geophys Res* 117:1–17. <https://doi.org/10.1029/2011JE003919>
- Cloete M, Hart RJ, Schmid HK, Drury M, Demanet CM, Sankar KV (1999) Characterization of magnetite particles in shocked quartz by means of electron- and magnetic force microscopy: Vredefort, South Africa. *Contrib Mineral Petrol* 137:232–245. <https://doi.org/10.1007/s004100050548>
- Coe RS, Paterson MS (1969) The  $\alpha$ - $\beta$  inversion in quartz: a coherent phase transition under nonhydrostatic stress. *J Geophys Res* 74:4921–4948. <https://doi.org/10.1029/jb074i020p04921>
- Compston W, Kröner A (1988) Multiple zircon growth within early archaean tonalitic gneiss from the ancient gneiss complex, Swaziland. *Earth Planet Sci Lett* 87:13–28. [https://doi.org/10.1016/0012-821X\(88\)90061-1](https://doi.org/10.1016/0012-821X(88)90061-1)
- Corner B, Durrheim RJ, Nicolaysen LO (1990) Relationships between the Vredefort structure and the Witwatersrand basin within the tectonic framework of the Kaapvaal craton as interpreted from regional gravity and aeromagnetic data. *Tectonophysics* 171:49–61. [https://doi.org/10.1016/0040-1951\(90\)90089-Q](https://doi.org/10.1016/0040-1951(90)90089-Q)
- de Wit MJ, de Ronde CEJ, Tredoux M, Roering C, Hart RJ, Armstrong RA, Green RWE, Peberdy E, Hart RA (1992) Formation of an Archean continent. *Nature* 357:553–562. <https://doi.org/10.1038/357553a0>
- Deer WA, Howie RA, Zussman J (2013) An introduction to the rock-forming minerals, 3rd edn. Berfords Information Press, Stevenage
- Dressler BO, Reimold WU (2004) Order or chaos? Origin and mode of emplacement of breccias in floors of large impact structures. *Earth Sci Rev* 67:1–54. <https://doi.org/10.1016/j.earscirev.2004.01.007>
- Ebert M, Poelchau MH, Kenkmann T, Schuster B (2020) Tracing shock-wave propagation in the Chicxulub crater: implications for the formation of peak rings. *Geology* 48:814–818. <https://doi.org/10.1130/G47129.1>
- Eriksson G, Pelton AD (1993) Critical evaluation and optimization of the thermodynamic properties and phase diagrams of the CaO–Al<sub>2</sub>O<sub>3</sub>, Al<sub>2</sub>O<sub>3</sub>–SiO<sub>2</sub>, and CaO–Al<sub>2</sub>O<sub>3</sub>–SiO<sub>2</sub> systems. *Metall Trans B* 24:807–816. <https://doi.org/10.1007/BF02663141>
- Ferrière L, Morrow JR, Amgaa T, Koeberl C (2009) Systematic study of universal-stage measurements of planar deformation features in shocked quartz: implications for statistical significance and representation of results. *Meteor Planet Sci* 44:925–940. <https://doi.org/10.1111/j.1945-5100.2009.tb00778.x>
- French BM, Koeberl C (2010) The convincing identification of terrestrial meteorite impact structures: what works, what doesn't, and why. *Earth Sci Rev* 98:123–170. <https://doi.org/10.1016/j.earscirev.2009.10.009>
- Frick C (1973) Kimberlitic Ilmenites. *South African. J Geol* 76:85–94
- Fricke A, Medenbach O, Schreyer W (1990) Fluid inclusions, planar elements and pseudotachylites in the basement rocks of the

- Vredefort structure, South Africa. *Tectonophysics* 171:169–183. [https://doi.org/10.1016/0040-1951\(90\)90097-R](https://doi.org/10.1016/0040-1951(90)90097-R)
- Galwey AK, Brown ME (1999) Thermal decomposition of ionic solids. Elsevier Sci. [https://doi.org/10.1016/S0167-6881\(99\)X8001-3](https://doi.org/10.1016/S0167-6881(99)X8001-3)
- Gibson RL (2019) The mesoarchaean basement complex of the Vredefort dome—a mid-crustal section through the central Kaapvaal craton exposed by impact. In: Kröner A, Hofmann A (eds) *The archaean geology of the Kaapvaal Craton, Southern Africa*. Springer Nature, Switzerland, pp 109–132. [https://doi.org/10.1007/978-3-319-78652-0\\_5](https://doi.org/10.1007/978-3-319-78652-0_5)
- Gibson RL, Armstrong RA, Reimold WU (1997) The age and thermal evolution of the Vredefort impact structure: a single-grain U-Pb zircon study. *Geochim Cosmochim Acta* 61:1531–1540. [https://doi.org/10.1016/S0016-7037\(97\)00013-6](https://doi.org/10.1016/S0016-7037(97)00013-6)
- Gibson RL, Reimold WU, Stevens G (1998) Thermal-metamorphic signature of an impact event in the Vredefort dome, South Africa. *Geology* 26:787–790. [https://doi.org/10.1130/0091-7613\(1998\)026%3c0787:TMSOAI%3e2.3.CO;2](https://doi.org/10.1130/0091-7613(1998)026%3c0787:TMSOAI%3e2.3.CO;2)
- Gibson RL, Reimold WU (2005) Shock pressure distribution in the Vredefort impact structure, South Africa. *Spec Pap Geol Soc Am* 384:329–349. <https://doi.org/10.1130/0-8137-2384-1.329>
- Gibson RL, Wallmach T (1995) Low pressure-high temperature metamorphism in the Vredefort Dome, South Africa: anticlockwise pressure-temperature path followed by rapid decompression. *Geol J* 30:319–331. <https://doi.org/10.1002/gj.3350300311>
- Gijben M (2012) The lightning climatology of South Africa. *S Afr J Sci* 108:1–10. <https://doi.org/10.4102/sajs.v108i3/4.740>
- Gilder SA, Pohl J, Eitel M (2018) Magnetic signatures of terrestrial meteorite impact craters: a summary. In: Lühr H, Wicht J, Gilder SA, Holschneider M (eds) *Magnetic fields in the solar system-planets, moons and solar wind interactions*. Springer, Cham, pp 357–382. [https://doi.org/10.1007/978-3-319-64292-5\\_13](https://doi.org/10.1007/978-3-319-64292-5_13)
- Grieve RAF, Coderre JM, Robertson PB, Alexopoulos J (1990) Microscopic planar deformation features in quartz of the Vredefort structure: anomalous but still suggestive of an impact origin. *Tectonophysics* 171:185–200. [https://doi.org/10.1016/0040-1951\(90\)90098-S](https://doi.org/10.1016/0040-1951(90)90098-S)
- Haggerty SE (1991) Oxide textures—a mini-atlas. *Rev Mineral* 25:129–219. <https://doi.org/10.1515/9781501508684-008>
- Hargraves RB (1970) Paleomagnetic evidence relevant to the origin of the Vredefort ring. *J Geol* 78:253–263. <https://doi.org/10.1086/627516>
- Harrison RJ, Becker U, Redfern SAT (2000) Thermodynamics of the R3 to R3c phase transition in the ilmenite-hematite solid solution. *Am Mineral* 85:1694–1705. <https://doi.org/10.2138/am-2000-11-1213>
- Hart RJ, Andreoli MAG, Smith CB, Otter ML, Durrheim R (1990) Ultramafic rocks in the centre of the Vredefort structure (South Africa): possible exposure of the upper mantle? *Chem Geol* 83:233–248. [https://doi.org/10.1016/0009-2541\(90\)90282-C](https://doi.org/10.1016/0009-2541(90)90282-C)
- Hart RJ, Andreoli MAG, Reimold WU, Tredoux M (1991) Aspects of the dynamic and thermal metamorphic history of the Vredefort cryptoexplosion structure: implications for its origin. *Tectonophysics* 192:313–331. [https://doi.org/10.1016/0040-1951\(91\)90106-3](https://doi.org/10.1016/0040-1951(91)90106-3)
- Hart RJ, Hargraves RB, Andreoli MAG, Tredoux M, Doucoure CM (1995) Magnetic anomaly near the center of the Vredefort structure: implications for impact-related magnetic signatures. *Geology* 23:277–280. [https://doi.org/10.1130/0091-7613\(1995\)023%3c0277:MANTCO%3e2.3.CO;2](https://doi.org/10.1130/0091-7613(1995)023%3c0277:MANTCO%3e2.3.CO;2)
- Hart RJ, Moser DE, Andreoli M (1999) Archean age for the granulite facies metamorphism near the center of the Vredefort structure, South Africa. *Geology* 27:1091–1094. [https://doi.org/10.1130/0091-7613\(1999\)027%3c1091:AAFTGF%3e2.3.CO;2](https://doi.org/10.1130/0091-7613(1999)027%3c1091:AAFTGF%3e2.3.CO;2)
- Hart RJ, Connell SH, Cloete M, Maré L, Drury M, Tredoux M (2000) “Super magnetic” rocks generated by shock metamorphism from the centre of the Vredefort impact structure, South Africa. *S Afr J Geol* 103:151–155. <https://doi.org/10.2113/103.2.151>
- Hart RJ, McDonald I, Tredoux M, de Wit MJ, Carlson RW, Andreoli M, Moser DE, Ashwal LD (2004) New PGE and Re/Os-isotope data from lower crustal sections of the Vredefort Dome and a reinterpretation of its “crust on edge” profile. *S Afr J Geol* 107:173–184. <https://doi.org/10.2113/107.1-2.173>
- Heaney PJ, Veblen DR (1991) Observation and kinetic analysis of a memory effect at the  $\alpha$ - $\beta$  quartz transition. *Am Mineral* 76:1459–1466
- Henkel H, Reimold WU (1998) Integrated geophysical modelling of a giant, complex impact structure: anatomy of the Vredefort structure, South Africa. *Tectonophysics* 287:1–20. [https://doi.org/10.1016/S0040-1951\(98\)80058-9](https://doi.org/10.1016/S0040-1951(98)80058-9)
- Henkel H, Reimold WU (2002) Magnetic model of the central uplift of the Vredefort impact structure, South Africa. *J Appl Geophys* 51:43–62. [https://doi.org/10.1016/S0926-9851\(02\)00214-8](https://doi.org/10.1016/S0926-9851(02)00214-8)
- Huffman AR, Brown JM, Carter NL, Reimold WU (1993) The microstructural response of quartz and feldspar under shock loading at variable temperatures. *J Geophys Res.* <https://doi.org/10.1029/93jb01425>
- Huffman AR, Reimold WU (1996) Experimental constraints on shock-induced microstructures in naturally deformed silicates. *Tectonophysics* 256:165–217. [https://doi.org/10.1016/0040-1951\(95\)00162-x](https://doi.org/10.1016/0040-1951(95)00162-x)
- Kaliwoda M, Giordano D, Krüger ME, Uysal I, Akmaz MR, Hoffmann V, Hochleitner R, Schmahl WW (2021) Raman spectroscopy as a tool for the quantitative estimate of chromium aluminium oxide content in chromite. *Spectroscopy* 36:17–23
- Kamo SL, Reimold WU, Krogh TE, Colliston WP (1996) A 2.023 Ga age for the Vredefort impact event and a first report of shock metamorphosed zircons in pseudotachylitic breccias and Granophyre. *Earth Planet Sci Lett* 144:369–387. [https://doi.org/10.1016/S0012-821X\(96\)00180-x](https://doi.org/10.1016/S0012-821X(96)00180-x)
- Killick AM, Reimold WU (1990) Review of the pseudotachylites in and around the Vredefort “Dome”, South Africa”. *S Afr J Geol* 93:350–365
- Kletetschka G, Acuna MH, Kohout T, Wasilewski PJ, Connery JEP (2004) An empirical scaling law for acquisition of thermoremanent magnetization. *Earth Planet Sci Lett* 226:521–528. <https://doi.org/10.1016/j.epsl.2004.08.001>
- Koenigsberger JG (1938) Natural residual magnetism of eruptive rocks—Part I. *Terr Magn Atmos Electr* 43:119–130
- Lana C, Gibson RL, Kisters AFM, Reimold WU (2003) Archean crustal structure of the Kaapvaal craton, South Africa—evidence from the Vredefort dome. *Earth Planet Sci Lett* 206:133–144. [https://doi.org/10.1016/S0012-821X\(02\)01086-5](https://doi.org/10.1016/S0012-821X(02)01086-5)
- Lana C, Reimold WU, Gibson RL, Koeberl C, Siegesmund S (2004) Nature of the archaean midcrust in the core of the Vredefort Dome, central Kaapvaal Craton, South Africa. *Geochim Cosmochim Acta* 68:623–642. [https://doi.org/10.1016/S0016-7037\(00\)00447-2](https://doi.org/10.1016/S0016-7037(00)00447-2)
- Langenhorst F, Deutsch A (1994) Shock experiments on pre-heated  $\alpha$ - and  $\beta$ -quartz: I. Optical and density data. *Earth Planet Sci Lett* 125:407–420. [https://doi.org/10.1016/0012-821X\(94\)90229-1](https://doi.org/10.1016/0012-821X(94)90229-1)
- Leroux H, Reimold WU, Doukhan JC (1994) A TEM investigation of shock metamorphism in quartz from the Vredefort dome, South Africa. *Tectonophysics* 230:223–239. [https://doi.org/10.1016/0040-1951\(94\)90137-6](https://doi.org/10.1016/0040-1951(94)90137-6)
- Lilly PA (1981) Shock metamorphism in the Vredefort Collar: evidence for internal shock sources. *J Geophys Res Solid Earth* 86:10689–10700. <https://doi.org/10.1029/JB086iB11p10689>
- Lindsley DH (1991) Experimental studies of oxide minerals. In: Lindsley DH (ed) *Oxide minerals: petrologic and magnetic significance*. De Gruyter, Berlin, Boston



- Markgraaff J (1986) Elastic behavior of quartz during stress induced Dauphiné twinning. *Phys Chem Miner* 13:10–112. <https://doi.org/10.1007/BF00311900>
- Martini JEJ (1978) Coesite and stishovite in the Vredefort Dome, South Africa. *Nature* 272:715–717
- Martini JEJ (1991) The nature, distribution and genesis of the coesite and stishovite associated with the pseudotachylite of the Vredefort Dome, South Africa. *Earth Planet Sci Lett* 103:285–300. [https://doi.org/10.1016/0012-821X\(91\)90167-G](https://doi.org/10.1016/0012-821X(91)90167-G)
- Martini JEJ (1992) The metamorphic history of the Vredefort dome at approximately 2 Ga as revealed by coesite-stishovite-bearing pseudotachylites. *J Metamorph Geol* 10:517–527. <https://doi.org/10.1111/j.1525-1314.1992.tb00102.x>
- McCarthy T, Stanistreet I, Robb L (1990) Geological studies related to the origin of the Witwatersrand Basin and its mineralization—an introduction and a strategy for research and exploration. *S Afr J Geol* 93:1–4
- Melosh HJ (1989) *Impact cratering: a geologic process*. Oxford University Press, New York
- Mernagh TP (1991) Use of the laser Raman microprobe for discrimination amongst feldspar minerals. *J Raman Spectrosc* 22:453–457. <https://doi.org/10.1002/jrs.1250220806>
- Migault A (1998) Concepts of shock waves. In: Benest D, Froeschle C (eds) *Impacts on earth*. Springer, Berlin, pp 79–112. [https://doi.org/10.1007/978-3-540-69703-9\\_5](https://doi.org/10.1007/978-3-540-69703-9_5)
- Minkin JA, Chao ECT (1971) Single crystal X-ray investigation of deformation in terrestrial and lunar ilmenite. In: *Proceedings of the second lunar science conference*. MIT Press, USA, pp 237–246
- Mohr-Westheide T, Reimold WU (2010) Microchemical investigation of small-scale pseudotachylitic breccias from the Archean gneiss of the Vredefort Dome, South Africa. In: Gibson RL, Reimold WU (eds) *Large meteorite impacts and planetary evolution IV*. Geological Society of America Special Paper 465, USA, pp 619–643. [https://doi.org/10.1130/2010.2465\(30\)](https://doi.org/10.1130/2010.2465(30))
- Morey GW, Bowen NL (1922) The melting of Potash Feldspar. *Am J Sci* 4:1–21
- Muundjua M, Hart RJ, Gilder SA, Carporzen L, Galdeano A (2007) Magnetic imaging of the Vredefort impact crater, South Africa. *Earth Planet Sci Lett* 261:456–468. <https://doi.org/10.1016/j.epsl.2007.07.044>
- Nakamura N, Hirose T, Borradaile GJ (2002) Laboratory verification of submicron magnetite production in pseudotachylites: relevance for paleointensity studies. *Earth Planet Sci Lett* 201:13–18. [https://doi.org/10.1016/S0012-821X\(02\)00704-5](https://doi.org/10.1016/S0012-821X(02)00704-5)
- Nakamura N, Okuno K, Uehara M et al (2010) Coarse-grained magnetites in biotite as a possible stable remanence-carrying phase in Vredefort granites. In: Gibson RL, Reimold WU (eds) *Large meteorite impacts and planetary evolution IV*. Geological Society of America Special Paper 465, USA, pp 165–172. [https://doi.org/10.1130/2010.2465\(11\)](https://doi.org/10.1130/2010.2465(11))
- Nel LT (1927) *Geological map of the country around Vredefort, scale 1:63360*, Union of South Africa, Department of Mines and Industries. Geological Survey, Pretoria
- Nesterenko VF (2001) *Dynamics of heterogeneous materials*. Springer, New York
- Perchuk LL, Tokarev DA, Van Reenen DD, Varlamov DA, Gerya TV, Sazonova LV, Fel'dman VI, Smit CA, Brink MC, Bischoff AA (2002) Dynamic and thermal history of the Vredefort explosion structure in the Kaapvaal craton, South Africa. *Petrology* 10:395–432
- Phillips M, Bussell MA, McDonald I, Hart RJ, Andreoli M (1999) A remote sensing and geological investigation of the Vredefort impact structure (South Africa) using landsat thematic mapper imagery. *Abstr Meteor Planet Sci* 34:A92–A93
- Pilkington M, Grieve RAF (1992) The geophysical signature of terrestrial impact craters. *Rev Geophys* 30:161–181. <https://doi.org/10.1029/92RG00192>
- Pilkington M, Hildebrand AR (2000) Three-dimensional magnetic imaging of the Chicxulub Crater. *J Geophys Res Solid Earth* 105:23479–23491. <https://doi.org/10.1029/2000jb900222>
- Plado J, Pesonen LJ, Puura V (1999) Effect of erosion on gravity and magnetic signatures of complex impact structures: geophysical modeling and applications. In: Dressler BO, Sharpton VL (eds) *Special Paper of the Geological Society of America*. Geological Society of America, Boulder, pp 229–239. <https://doi.org/10.1130/0-8137-2339-6.229>
- Poelchau MH, Kenkmann T (2011) Feather features: a low-shock-pressure indicator in quartz. *J Geophys Res* 116:1–13. <https://doi.org/10.1029/2010JB007803>
- Pohl J, Poschold K, Reimold WU, Meyer C, Jacob J (2010) Ries crater, Germany: the Enkingen magnetic anomaly and associated drill core SUBO 18. In: Gibson RL, Reimold WU (eds) *Large meteorite impacts and planetary evolution IV*. Geological Society of America Special Paper 465, USA, pp 141–163. [https://doi.org/10.1130/2010.2465\(10\)](https://doi.org/10.1130/2010.2465(10))
- Rakov VA, Uman MA (2003) *Lightning: physics and effects*. Cambridge University Press, Cambridge. <https://doi.org/10.1063/1.1878338>
- Rankin GA (1915) The ternary system CaO–Al<sub>2</sub>O<sub>3</sub>–SiO<sub>2</sub>, with optical study by F. E. Wright. *Am J Sci* 39:1–79. <https://doi.org/10.2475/ajs.s4-39.229.1>
- Reimold WU (1990) The controversial microdeformations in quartz from the Vredefort structure, South Africa—a discussion. *S Afr J Geol* 93:645–663
- Reimold WU, Gibson RL (2005) “Pseudotachylites” in large impact structures. In: Koeberl C, Henkel H (eds) *Impact tectonics*. Springer, Berlin, pp 1–53. [https://doi.org/10.1007/3-540-27548-7\\_1](https://doi.org/10.1007/3-540-27548-7_1)
- Reimold WU, Gibson RL (2006) The melt rocks of the Vredefort impact structure—Vredefort Granophyre and pseudotachylitic breccias: implications for impact cratering and the evolution of the Witwatersrand Basin. *Chem Erde* 66:1–35. <https://doi.org/10.1016/j.chemer.2005.07.003>
- Reimold WU, Hoffmann M, Hauser N, Schmitt RT, Zaag PT, Mohr-Westheide T (2016) A geochemical contribution to the discussion about the genesis of impact-related pseudotachylitic breccias: studies of PTB in the Otavi and Kudu Quarries of the Vredefort Dome support the “In Situ Formation” hypothesis. *S Afr J Geol* 119:453–472. <https://doi.org/10.2113/gssajg.119.3.453>
- Reynolds IM (1984) Tectonically deformed ilmenite in titaniferous iron ores of the Mambula Complex, Zululand, South Africa. *Can Mineral* 22:411–416
- Reznik B, Kontny A, Fritz J (2017) Effect of moderate shock waves on magnetic susceptibility and microstructure of a magnetite-bearing ore. *Meteor Planet Sci* 52:1495–1504. <https://doi.org/10.1111/maps.12787>
- Reznik B, Kontny A, Gerhards U (2016) Shock-induced deformation phenomena in magnetite and their consequences on magnetic properties. *Geochem Geophys Geosyst* 17:2374–2393. <https://doi.org/10.1002/2013GC005223>. Received
- Sakai H, Sunada S, Sakurano H (1998) Study of lightning current by remanent magnetization. *Electr Eng Jpn (english Transl Denki Gakkai Ronbunshi)* 123:41–47. [https://doi.org/10.1002/\(SICI\)1520-6416\(199806\)123:4%3c41::AID-EEJ6%3e3.0.CO;2-O](https://doi.org/10.1002/(SICI)1520-6416(199806)123:4%3c41::AID-EEJ6%3e3.0.CO;2-O)
- Salminen J, Pesonen LJ, Lahti K, Kannus K (2013) Lightning-induced remanent magnetization—the Vredefort impact structure, South Africa. *Geophys J Int* 195:117–129. <https://doi.org/10.1093/gji/ggt230>

- Salminen J, Pesonen LJ, Reimold WU, Donadini F, Gibson RL (2009) Paleomagnetic and rock magnetic study of the Vredefort impact structure and the Johannesburg Dome, Kaapvaal Craton, South Africa—Implications for the apparent polar wander path of the Kaapvaal Craton during the Mesoproterozoic. *Precambrian Res* 168:167–184. <https://doi.org/10.1016/j.precamres.2008.09.005>
- Schreyer W (1983) Metamorphism and fluid inclusions in the basement of the Vredefort dome, South Africa: guidelines to the origin of the structure. *J Petrol* 24:26–47. <https://doi.org/10.1093/petrology/24.1.26>
- Schreyer W, Medenbach O (1981) CO<sub>2</sub>-rich fluid inclusions along planar elements of quartz in basement rocks of the Vredefort Dome, South Africa. *Contrib Mineral Petrol* 77:93–100. <https://doi.org/10.1007/BF00636513>
- Sciar CB, Bauer JF, Pickart SJ, Alperin HA (1973) Shock effects in experimentally shocked terrestrial ilmenite, lunar ilmenite of rock fragments in 1–10 mm fines (10085,19), and lunar rock 60015,127. In: *Proceedings of the fourth lunar science conference*. Pergamon Press, Houston, pp 841–859
- Scott RG, Pilkington M, Tanczyk EI (1997) Magnetic investigations of the West Hawk, Deep Bay and Clearwater impact structures, Canada. *Meteor Planet Sci* 32:293–308. <https://doi.org/10.1111/j.1945-5100.1997.tb01267.x>
- Sharp TG, DeCarli PS (2006) Shock effects in meteorites. In: Lauretta DS, McSween HY (eds) *Meteorites and the early solar system II*. University of Arizona Press, USA, pp 653–677. <https://doi.org/10.2307/j.ctv1v7zdm>
- Shimada M (1969) Melting of albite at high pressures in the presence of water. *Earth Planet Sci Lett* 6:447–450. [https://doi.org/10.1016/0012-821X\(69\)90114-9](https://doi.org/10.1016/0012-821X(69)90114-9)
- Shimizu H, Koyama T, Koyama S, Utada H (2007) A geomagnetic total intensity anomaly originated from lightning-induced isothermal remanent magnetization: case of the Yatsugatake Magnetic Observatory, central Japan. *Earth Planets Sp* 59:141–149. <https://doi.org/10.1186/BF03352687>
- Spray JG (1992) A physical basis for the frictional melting of some rock-forming minerals. *Tectonophysics* 204:205–221. [https://doi.org/10.1016/0040-1951\(92\)90308-S](https://doi.org/10.1016/0040-1951(92)90308-S)
- Spray JG (1995) Pseudotachylite controversy: fact or friction? *Geology* 23:1119–1122. [https://doi.org/10.1130/0091-7613\(1995\)023%3c1119:PCFOF%3e2.3.CO;2](https://doi.org/10.1130/0091-7613(1995)023%3c1119:PCFOF%3e2.3.CO;2)
- Spray JG (2010) Frictional melting processes in planetary materials: from hypervelocity impact to earthquakes. *Annu Rev Earth Planet Sci* 38:221–254. <https://doi.org/10.1146/annurev.earth.031208.100045>
- Spray JG, Biren MB (2021) Distinguishing friction-from shock-generated melt products in hypervelocity impact structures. In: Reimold WU, Koeberl C (eds) *Large meteorite impacts and planetary evolution VI*. Geological Society of America Special Paper 550, USA, pp 147–170. <https://doi.org/10.1130/SPE550>
- Steph D (1990) The geology and gravity field in the central core of the Vredefort structure. *Tectonophysics* 171:75–103. [https://doi.org/10.1016/0040-1951\(90\)90091-L](https://doi.org/10.1016/0040-1951(90)90091-L)
- Stöffler D, Grieve RAF (2007) Impactites. In: Fettes D, Desmons J (eds) *Metamorphic rocks: a classification and glossary of terms, recommendations of the international union of geological sciences*. Cambridge University Press, Cambridge. <https://doi.org/10.3749/canmin.45.6.1545>
- Stöffler D, Hamann C, Metzler K (2018) Shock metamorphism of planetary silicate rocks and sediments: proposal for an updated classification system. *Meteor Planet Sci* 53:5–49. <https://doi.org/10.1111/maps.12912>
- Stöffler D, Langenhorst F (1994) Shock metamorphism of quartz in nature and experiment: I. Basic observation and theory. *Meteoritics* 29:155–181. <https://doi.org/10.1111/j.1945-5100.1994.tb00670.x>
- Tada T, Kurosawa K, Ono H, Hamann C, Okamoto T, Niihara T, Matsui T (2022) Shock recovery of granite with a decaying shock wave: feather features formation in quartz. In: *Abstract of 52nd Lun and Planet Sci Conf*, pp 1733
- Tan W, He H, Wang CY, Dong H, Liang X, Zhu J (2016) Magnetite exsolution in ilmenite from the Fe–Ti oxide gabbro in the Xinjie intrusion (SW China) and sources of unusually strong remnant magnetization. *Am Mineral* 101:2759–2767. <https://doi.org/10.2138/am-2016-5688>
- Therriault AM, Grieve RAF, Reimold WU (1997) Original size of the Vredefort structure: implications for the geological evolution of the Witwatersrand Basin. *Meteor Planet Sci* 32:71–77. <https://doi.org/10.1111/j.1945-5100.1997.tb01242.x>
- Treppmann CA (2008) Shock effects in quartz: compression versus shear deformation—an example from the Rochechouart impact structure, France. *Earth Planet Sci Lett* 267:322–332. <https://doi.org/10.1016/j.epsl.2007.11.035>
- Treppmann CA, Spray JG (2005) Planar microstructures and Dauphiné twins in shocked quartz from the Charlevoix impact structure. In: Kenkmann T, Hörz F, Deutsch A (eds) *Large meteorite impacts III*. Geological Society of America Special Paper, Canada, pp 315–328. <https://doi.org/10.1130/0-8137-2384-1.315>
- Treppmann CA, Stöckert B, Dorner D, Moghadam RH, Küster M, Röller K (2007) Simulating coseismic deformation of quartz in the middle crust and fabric evolution during postseismic stress relaxation—an experimental study. *Tectonophysics* 442:83–104. <https://doi.org/10.1016/j.tecto.2007.05.005>
- Tröger WE (1982) Optische Bestimmung der gesteinsbildende Minerale. In: Bambauer H, Taborszky F, Trochim HD (eds) *E. Schweizerbart'sche Verlagsbuchhandlung*, Stuttgart
- Tromans D, Meech JA (2002) Fracture toughness and surface energies of minerals: theoretical estimates for oxides, sulphides, silicates and halides. *Miner Eng* 15:1027–1041. <https://doi.org/10.1016/j.mineng.2003.09.006>
- Tullis J (1970) Quartz: preferred orientation in rocks produced by dauphiné twinning. *Science* 168:1342–1344. <https://doi.org/10.1126/science.168.3937.1342>
- Ugalde HA, Artemieva N, Milkereit B (2005) Magnetization on impact structures - Constraints from numerical modeling and petrophysics. In: Kenkmann T, Hörz F, Deutsch A (eds) *Large Meteorite Impacts III*. Geological Society of America, Boulder, pp 25–42
- Verrier V, Rochette P (2002) Estimating peak currents at ground lightning impacts using remanent magnetization. *Geophys Res Lett* 29:2–5. <https://doi.org/10.1029/2002GL015207>
- Wenk HR, Chen K, Smith R (2011) Morphology and microstructure of magnetite and ilmenite inclusions in plagioclase from Adirondack anorthositic gneiss. *Am Mineral* 96:1316–1324. <https://doi.org/10.2138/am.2011.3760>
- Whitney DL, Broz ME, Cook RF (2007) Hardness, toughness, and modulus of some common metamorphic minerals. *Am Mineral* 92:281–288. <https://doi.org/10.2138/am.2007.2212>
- Zeh A, Gerdes A, Millonig L (2011) Hafnium isotope record of the Ancient Gneiss Complex, Swaziland, southern Africa: evidence for Archaean crust-mantle formation and crust reworking between 3.66 and 2.73 Ga. *J Geol Soc Lond* 168:953–963. <https://doi.org/10.1144/0016-76492010-117>

**Publisher's Note** Springer Nature remains neutral with regard to jurisdictional claims in published maps and institutional affiliations.